SIAM J. Applied Dynamical Systems
Vol. 9, No. 3, pp. 1019–1060

Spatially Localized Synchronous Oscillations in Synaptically Coupled Neuronal Networks: Conductance-based Models and Discrete Maps*

Stefanos E. Folias† and G. Bard Ermentrout†

Abstract. We study the qualitative behavior of localized synchronous oscillations organized by synaptic inhibition in two types of spatially extended neuronal network models driven by a time-independent, localized excitatory input. Each network is formulated as a one-dimensional network of conductance-based models constituting a high-dimensional dynamical system of nonlocal differential equations. Although such equations readily generate highly complex dynamic behavior, in the case of strong inhibitory coupling the response of the network to a localized Gaussian input is a solution in which a single, continuous band of cells fire nearly synchronous action potentials, in an approximately periodic fashion in time. Tracking the cycle-to-cycle evolution of the width of the band of synchronous action potentials reveals the characteristic behavior of low-dimensional, discrete dynamical systems. Based upon a continuum formulation of the conductance-based model, we heuristically develop and analyze one- and two-dimensional implicit discrete maps for both a purely inhibitory and an excitatory-inhibitory network of neurons. Although the discrete maps do not predict the band widths precisely, they generally reflect the qualitative behavior of the conductance-based model. The most salient features of the bifurcations of fixed points to period 2 orbits and resonances indicate that in some cases these high-dimensional continuous dynamical systems exhibit behavior which can be captured in related low-dimensional discrete maps. Finally, we describe a global bifurcation in the discrete map for the excitatory-inhibitory network in which a strong (1:2) resonance bifurcation occurs on a period 2 orbit, giving rise to a pair of double homoclinic tangles that generate nontrivial dynamics.

Key words. synchronous oscillation, spatially extended neural networks, reduction to discrete maps, localized activity, bifurcation theory, strong resonance, generalized dynamical system

AMS subject classifications. 92C20, 37L99, 37E99

DOI. 10.1137/090780092

1. Introduction.

Synchronous fast oscillations in the brain are believed to be important for sensory processing, attention, binding assemblies of neurons, and motor tasks. In vitro experimental models in conjunction with mathematical modeling have demonstrated that synaptic inhibition is a primary mechanism capable of synchronizing neurons within the *beta* and *gamma* frequency bands spanning 20–100 Hz [27, 25, 28]. Populations of neurons in the cortex, for example, can engage in stimulus-evoked, synchronous gamma oscillations in which synchronous oscillations arise in the cortical network in response to a nonoscillatory stimulus input from the lateral geniculate nucleus of the thalamus [13]. Synchronous gamma oscillations have been used in a network of neurons in which the localized oscillation encodes the orientation of a stimulus in a model of working memory [6]. In firing-rate neural networks

*Received by the editors December 14, 2009; accepted for publication (in revised form) by T. Kaper June 30, 2010; published electronically September 7, 2010. This work was supported by NSF grants EMSW21-RTG 0739261 and DMS-0817131.
http://www.siam.org/journals/siads/9-3/78009.html
†Department of Mathematics, University of Pittsburgh, Pittsburgh, PA 15260 (stefanos@pitt.edu, bard@pitt.edu).

models of Wilson–Cowan type it has been shown that a persistent, localized stimulus can give rise to both stationary and oscillatory pulses of persistent activity that is localized about the input [10, 29]. Synaptic inhibition was additionally found to generate nontrivial spatiotemporal patterns of coherent oscillations [11]. However, this class of firing-rate models is best suited for asynchronous activity and is currently unable to address the temporally correlated inputs that arise during synchronous oscillations.

Along these lines, we examine a simple case of stimulus-evoked synchronous oscillations arising from a localized current input in a network of neurons that synchronizes via synaptic inhibition. The localized input causes a local population of neurons to fire action potentials repetitively. Strong synaptic inhibition effectively synchronizes these cells, by first inhibiting the cells temporarily from firing and subsequently allowing them to fire during a short window of opportunity before the next wave of inhibition. The decay of the inhibitory synaptic currents is usually exponential in fashion, and the time constant of decay sets the period of the oscillation [28]. By synchronizing itself, the inhibitory population can synchronize the excitatory population through the same oscillatory synaptic inhibition. The excitatory population can, in turn, drive the inhibitory population to maintain an oscillation (PING mechanism). Alternatively, the population of inhibitory interneurons can be driven by a strong input to generate a synchronous oscillation (ING mechanism). *(PING/ING are acronyms for pyramidal–interneuronal network gamma* [28, 5]*. The inclusion of "P" implies that the excitatory synaptic currents are necessary for the gamma oscillation.)*

In section 2, we examine synchronized oscillations in Hodgkin–Huxley-type conductance-based models. We consider both a synaptically coupled inhibitory network and an excitatory-inhibitory network, in which the synchronous oscillations are localized about a time-independent, Gaussian-like input that excites a local region of cells along a one-dimensional spatial domain. In numerical simulations of either network, strong, distance-dependent inhibitory coupling resulted in a single, continuous band (interval) of neurons firing nearly synchronous action potentials at gamma frequencies. The cycle-by-cycle evolution of the width of this band of action potentials readily approached steady solutions either as a fixed width or an alternation between two widths, suggesting that the dynamics may be captured by low-dimensional discrete maps. Indeed, in a variety of different neuronal models, the reduction to low-dimensional discrete dynamical systems has proved an effective technique for gaining insight into the behavior of complex models [9, 21, 22, 7, 20].

In section 3 for the inhibitory population only and in section 4 for the excitatory-inhibitory population, we heuristically derive and analyze one- and two-dimensional discrete maps, whose iterates define the cycle-by-cycle variation in the width of the band of spiking cells by taking into account the decay and spatial extent of the synaptic inhibition (and excitation) generated during each cycle. Using linear stability analysis and numerical simulations, we make qualitative comparisons between the conductance-based models and the discrete maps, demonstrating that some of the qualitative features of the oscillations arising in the high/infinite-dimensional conductance-based models may be captured in terms of the solutions of low-dimensional discrete maps. Finally, in section 4.4 in a two-dimensional discrete map for the excitatory-inhibitory population, we demonstrate a global bifurcation in which a strong (1:2) resonance bifurcation occurs on a period 2 orbit, giving rise to a pair of double homoclinic tangles that generate nontrivial dynamics.

2. Localized synchronous oscillations in conductance-based models. We briefly describe a family of spatially extended, conductance-based models and a class of simple and regular spiking behavior exhibited in numerical simulations in which strong inhibitory synaptic coupling governs the oscillatory response of the network to a constant input localized in space. By spatially extended, we mean that we extend the nonlinear ordinary differential equations that govern the evolution of a conductance-based model for a single neuron by introducing synaptic coupling between pairs of cells with a strength of interaction that is dependent upon the spatial location of the cells. To model large populations of neurons, as a simplification, one typically collapses the entire spatial structure of each neuron to a single isopotential compartment, effectively representing the membrane potential in the cell body or axon. The combination of the reliable transmission of the action potential from near the cell body to the synapses and the segregation of two cells at a chemical synapse motivates this approximation. Consequently, these models can be seen to describe the membrane fluctuations and action potentials generated in patches of the membrane of the neuronal cell bodies. These spatially extended neuronal models are high-dimensional dynamical systems which are continuous in time and discrete in space. The cells in the network, ordered according to their spatial location, are naturally amenable to numerical simulation.

We begin in section 2.1 by describing the conductance-based models for a network of neurons which is formed from two populations, one of excitatory neurons and the other inhibitory neurons, with each population synaptically coupled to itself as well as the other population. We subsequently describe numerical results of this model in two distinct cases: (i) an *inhibitory* network, in which the coupling between the excitatory and inhibitory populations is turned off and the excitatory population is neglected altogether, and (ii) an *excitatory-inhibitory* network, with the full range of synaptic coupling between the populations. In both cases, the network is being driven by a time-independent, spatially localized, excitatory current input. We demonstrate that, in the case of strong inhibition, the two systems exhibit spatially localized, periodic oscillations in the form of finite, continuous bands of cells firing synchronously and periodically. Interestingly, we show that the cycle-by-cycle spatial extent (width) of the bands of spiking neurons often approaches steady behavior characteristic of a fixed point in a discrete map, or an alternation of widths characteristic of a flip bifurcation to a period 2 orbit. This motivates the approach taken in sections 3 and 4 to describe these spatially organized periodic oscillations in terms of one- and two-dimensional discrete dynamical systems. These discrete maps, however, are developed most naturally from a spatial continuum description of the conductance-based model that is commensurate with the discrete spatial model.

Numerical simulations of the conductance-based model involving high-dimensional spatial discretizations indicate that strong inhibition is necessary to ensure that the behavior is regular, i.e., nearly synchronous and periodic. Over a range of moderately strong inhibition, a band of synchronous activity exhibits small fluctuations in its spatial extent, although, overall, it can be roughly characteristic of fixed points and period 2 orbits. Decreasing inhibition degrades the synchrony sufficiently that the activity gradually breaks up, leading to significantly more complex spatiotemporal behavior. In the excitatory-inhibitory model, a balance of excitation and inhibition is necessary to maintain this regular behavior. In this article, we restrict our focus to the most regular and nearly synchronous oscillations produced by sufficiently strong inhibition in the conductance-based models.

2.1. One-dimensional network model for an excitatory-inhibitory population. As a basic unit, a *conductance-based model* is an n-dimensional system of ordinary differential equations that describes the evolution of the membrane potential of neurons in terms of only the dynamics of various ionic currents across the cellular membrane. This basic unit is then taken to represent the dynamics for a single neuron, and each of the two populations is composed of neurons at discrete points x_k, uniformly distributed along one spatial dimension and denoted by the spatial index k. Each population forms distance-dependent synaptic coupling to neurons within its population as well as to neurons in the other population, thereby forming a mutually coupled network. We assume that the system has a stable steady state in the absence of inputs or coupling and represents an excitable medium rather than an oscillatory medium.

Consider the *spatially extended conductance-based model* for a synaptically coupled excitatory-inhibitory population:

$$
\begin{aligned}
C\frac{dv_e}{dt}(x_k,t) &= -I_e^{\mathsf{ion}}(v_e,m_e,n_e,h_e) - I_e^{\mathsf{syn}}(x_k,t) + I_e^{\mathsf{input}}(x_k),\\
C\frac{dv_i}{dt}(x_k,t) &= -I_i^{\mathsf{ion}}(v_i,m_i,n_i,h_i) - I_i^{\mathsf{syn}}(x_k,t) + I_i^{\mathsf{input}}(x_k),\\
\tau_{q_e}\big(v_e(x_k,t)\big)\frac{dq_e}{dt}(x_k,t) &= q_e^{\infty}\big(v_e(x_k,t)\big) - q_e(x_k,t), \qquad q_e \in \{m_e,h_e,n_e\},\\
\tau_{q_i}\big(v_i(x_k,t)\big)\frac{dq_i}{dt}(x_k,t) &= q_i^{\infty}\big(v_i(x_k,t)\big) - q_i(x_k,t), \qquad q_i \in \{m_i,h_i,n_i\}.
\end{aligned}
\tag{2.1}
$$

Let $u\in\{e,i\}$ be a subscript identifying either the excitatory or inhibitory population. v_u represents the membrane potential of population u, and m_u, h_u, n_u the associated gating variables for the ionic conductances, which, for simplicity, is the family of four-dimensional models that include only the basic Na^+ and K^+ ionic currents responsible for action potential generation [16, 15]. We use identical kinetics for the ionic conductances in both populations, though some differences exist between these classes of neurons in the brain. The sum I_u^{ion} of the ionic currents intrinsic to each neuron is

$$
I_u^{\mathsf{ion}}(v_u,m_u,n_u,h_u) = g_{\mathrm{L}}\big(v_u - V_{\mathrm{L}}\big) + g_{\mathrm{K}}n_u^4\big(v_u - V_{\mathrm{K}}\big) + g_{\mathrm{Na}}m_u^3h_u\big(v_u - V_{\mathrm{Na}}\big).
$$

The gating variables m and h are the activation and inactivation variables for the Na^+ conductance, and n is the activation variable for the K^+ conductance. (The parameters and auxiliary functions used in our numerical simulations are listed in Appendix A.)

The time-dependent synaptic current $I_e^{\mathsf{syn}}(x_k,t)$, which is the total synaptic current received by the neuron at x_k in the excitatory population,

$$
\begin{aligned}
I_e^{\mathsf{syn}}(x_k,t) = g_{ee}^c \sum_j w_{ee}(x_k-x_j)s_e(x_j,t)\Big[\,v_e(x_k,t) - V_e^{\mathsf{syn}}\,\Big]\,\Delta x\\
+ g_{ei}^c \sum_j w_{ei}(x_k-x_j)\,s_i(x_j,t)\Big[\,v_e(x_k,t) - V_i^{\mathsf{syn}}\,\Big]\,\Delta x,
\end{aligned}
$$

is composed of a positive (excitatory) synaptic current with subscripts ee, representing the synaptic current from the excitatory population to itself, and a negative (inhibitory) synaptic

current with subscripts ei, representing the synaptic current from the inhibitory population to the excitatory population. The form of the spatial coupling is given by the weight functions $w_{uv}(x)$. The convention of the dual subscript order uv is for u to be the population *receiving* synaptic current and for v to represent the population *generating* the synaptic current. Whether the synaptic current is excitatory or inhibitory is determined by the sign of the difference $(v_u(x,t) - V_v^{\mathsf{syn}})$ between the membrane potential $v_u(x,t)$ of the postsynaptic cell u and the reversal potential V_v^{syn} for the synaptic current generated by the presynaptic cell v. The synaptic current to the inhibitory neuron at x_k is analogously given by

$$I_i^{\mathsf{syn}}(x_k,t) = g_{ie}^c \sum_j w_{ie}(x_k - x_j)\, s_e(x_j,t)\Big[\, v_i(x_k,t) - V_e^{\mathsf{syn}}\,\Big]\,\Delta x + g_{ii}^c \sum_j w_{ii}(x_k - x_j)\, s_i(x_j,t)\Big[\, v_i(x_k,t) - V_i^{\mathsf{syn}}\,\Big]\,\Delta x.$$

The dynamics of the excitatory synaptic gating variable s_e to both the excitatory and inhibitory populations are taken to be identical (similarly for s_i). The synaptic variable s_v, for the presynaptic population $v \in \{e,i\}$, evolves dynamically according to

$$\frac{ds_v}{dt}(x_k,t) = \alpha_v \kappa\big(v_v(x_k,t)\big)\Big(1 - s_v(x_k,t)\Big) - \beta_v s_v(x_k,t), \qquad v \in \big\{e,i\big\},$$

resulting in no synaptic current from population v if the membrane potential $v_v(x_k,t)$ is not elevated to spiking levels.

The inputs $I_u^{\mathsf{input}}(x)$ and normalized synaptic weights $w_{uv}(x)$ are taken to be positive, even-symmetric, $\mathcal{C}^1$ functions that monotonically decay to zero as $x \to \pm\infty$. The parameters g_{uv}^c and σ_{uv}^c represent the conductance strength and characteristic spatial extent of the weight functions w_{uv}^c, and I_i^c and σ_u^c represent the amplitude and spatial extent of the input current I_u^{input} to population $u \in \{e,i\}$. The superscript ^{c} differentiates parameters in the conductance-based model from related ones in the discrete maps in sections 3 and 4. Integrals of w_{uv} are normalized to 1 over $\mathbb{R}$ to relate this model to a continuum model on an infinite domain (see section 3.1). For simulations, we discretize time using an improved Euler scheme, and the number of spatial grid points was varied between 401 to 2001 with time step ranging from $\Delta t \in [10^{-4}, 10^{-2}]$. We take the synaptic weight and input functions to be Gaussians,

$$w_{uv}(x) = \frac{1}{\sqrt{\pi}\sigma_{uv}^c}\, e^{-\left(\frac{x}{\sigma_{uv}^c}\right)^2}, \qquad I_u^{\mathsf{input}}(x) = I_u^c\, e^{-\left(\frac{x}{\sigma_u^c}\right)^2}, \tag{2.2}$$

and consider excitatory input currents only ($I_e^c, I_i^c > 0$).

In the absence of synaptic coupling, the discrete equations decouple and evolve independently according to their respective input and ionic conductances. The region of asynchronously spiking neurons firing in response to the input is localized in space due to the decay of the input $I_u^{\mathsf{input}}(x)$ with distance from its center. We restrict the types of solutions we are studying to those in which the spatial extent of spiking neurons is sufficiently far from the edges of the domain. Although every neuron sees the synaptic currents due to the positivity of the weight functions, they are generated only by the neurons which undergo action potentials. Consequently, if the input and the response to the input are both localized in space, any

further extension of the spatial discretization beyond this spatial extent (1) does not affect the spiking region since no additional synaptic currents are produced and (2) only reveals the continued approach to the equilibrium values of all variables. This can be violated, for example, if the current input or synaptic excitation is too strong near the boundary.

While in some cases the domain may simply be extended to capture all the relevant spiking neurons, the excitatory coupling strength g^c_{ee} and characteristic spatial extent σ^c_{ee} determine whether strong positive feedback is propagated and regenerated through the excitatory-to-excitatory synaptic coupling, leading to runaway excitation that necessarily approaches the boundary. The combined nonlocal effects of both positive and negative feedback loops arising from the synaptic interactions between these two populations make it difficult to determine the conditions under which such localized activity can be guaranteed. We can intuitively say that, at one extreme, sufficiently strong inhibition extending over a sufficiently large region can maintain a bounded region of spiking in both the excitatory and inhibitory populations, and, at the other extreme, sufficiently weak excitation precludes the propagation of activity into regions where the input on its own is too weak to sustain spiking activity. (Runaway activity is further constrained in real neurons by additional processes, such as adaptation currents or synaptic depression.)

2.2. Synchronous oscillations in the inhibitory network. We now describe a class of simple spatiotemporal patterns exhibited by the model (2.1) for a network of strongly interacting inhibitory neurons in the presence of a localized, excitatory current input. The coupling between excitatory and inhibitory neurons is turned off, and the excitatory population is ignored altogether. Assuming that (i) the conductance-based model contains only the basic currents responsible for action potential generation, (ii) subthreshold inputs result in an approach to a stable equilibrium, and (iii) there are no excitatory synaptic interactions, the input is the only source of sustained excitation in the network. In the absence of inhibitory synaptic connections, the steady behavior of the system in response to a Gaussian input is illustrated in the rastergram in Figure 1(a), in which points graphed in the time-space domain correspond to the timing of action potentials, or *spikes*, in neurons located at those spatial points. Although rastergrams remove the precise temporal structure of the membrane potential, they capture the spatial extent and precise timing of all cells firing action potentials. With the synaptic coupling turned off, the rastergram illustrates a pattern in which a neuron at x periodically fires action potentials as a function of the constant current input $I^{\text{input}}(x)$. The frequency of oscillation is highest in the center and diminishes with distance until a threshold current for firing periodic action potentials is reached. Beyond this point, the neural medium is quiescent as the decay of the Gaussian input is unable to excite the medium. This essentially reflects what is commonly called the *FI-curve* of the single-cell model, depicting firing frequency (F) of periodic action potentials as a function of the *constant* current input (I). The FI-curve for a single-cell version of (2.1) is shown in Figure 6(a) for the parameters in Appendix A.

The inclusion of strong synaptic inhibition, by sufficiently increasing the conductance strength g^c_{ii}, can organize the cells to fire in a nearly synchronous and periodic fashion, as shown in Figure 1(b). The input I^{input}_i provides the strongest drive to the neurons at the center of the input. Once a critical mass of cells fire, a wave of inhibition ensues, having the immediate effect of preventing the firing of other cells nearing threshold that would otherwise fire. On a longer time scale, the decay of the inhibition determines which cells fire during

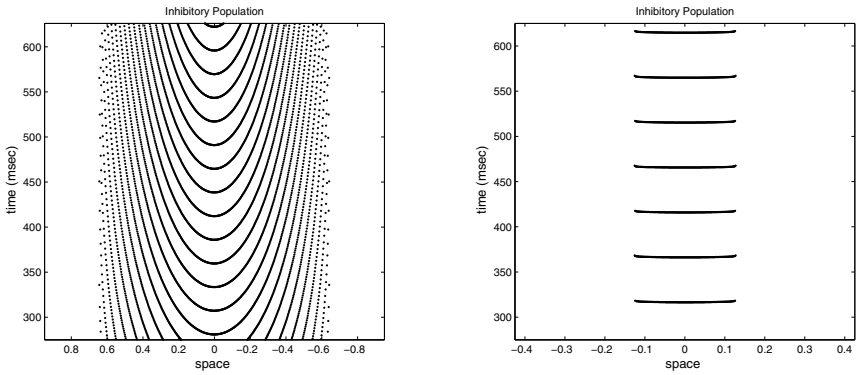

(a) No inhibition—$g_{ii}^c = 0.0$. (b) Strong inhibition—$g_{ii}^c = 5.0$.

Figure 1. *Spiking patterns in the inhibitory network in the presence of a localized Gaussian input.* (a) *With the inhibitory synaptic coupling turned off* ($g_{ii}^c = 0$)*, an input current amplitude* I_i^c *that is above threshold generates a localized region of spiking cells in which firing frequency decreases with distance from the center of the input. The borders of the region are determined by the minimum current needed to continually fire action potentials.* (b) *The same network and parameters as in* (a) *with strong inhibitory coupling* $g_{ii}^c = 5.0$ *produce a stationary band of neurons periodically firing nearly synchronous action potentials. Common parameters are* $I_i^c = 0.4$, $\sigma_i^c = 0.5$, $\sigma_{ii}^c = 1$.

the subsequent cycle. Strong inhibition effectively creates a narrow window in which the cells fire nearly synchronously. This is a localized example of ING [28] occurring in the network. Relaxing the inhibition diminishes the short-term effect and allows cells in the periphery to fire midcycle, disrupting synchrony and leading to more complex patterns of activity. We identify the beginning of each cycle of the oscillation with the initiation of the nearly synchronous band of action potentials. Subsequently, the interval of spiking cells $(-b_n^c, b_n^c)$, centered about the input, generates a wave of inhibition that prevents other cells from firing until the end of the nth cycle.

Generally, the inhibitory population tends to approach either a fixed width of cells firing on each cycle, as shown in Figure 1(b), or an alternation of a pair of distinct widths, as shown in Figure 2(a) (for inhibition sufficiently strong to prevent small fluctuations in the width). This motivates the approach taken in section 3, that the evolution of the width of the spiking region in (2.1) can be described by the attracting sets of a low-dimensional discrete map, in particular, as a fixed point or a *period* 2 *orbit* (a periodic orbit of a discrete map containing two points). We note, however, that the conductance-based model for the inhibitory network also exhibits other alternating spatial patterns characterized by disjoint intervals of synchronously spiking neurons separated by gaps of neurons which fire on the subsequent cycles. One such pattern, illustrated in Figure 2(b), bifurcates in a sharp transition from the solution in Figure 2(a) as the spatial extent σ_i^c of the input is increased. The formulation of the discrete maps in sections 3 and 4 assumes that each oscillation cycle is characterized by the firing of a single, continuous band of synchronously spiking neurons. The discrete maps would need to be modified for spatiotemporal patterns with gaps but would still be valid in such cases.

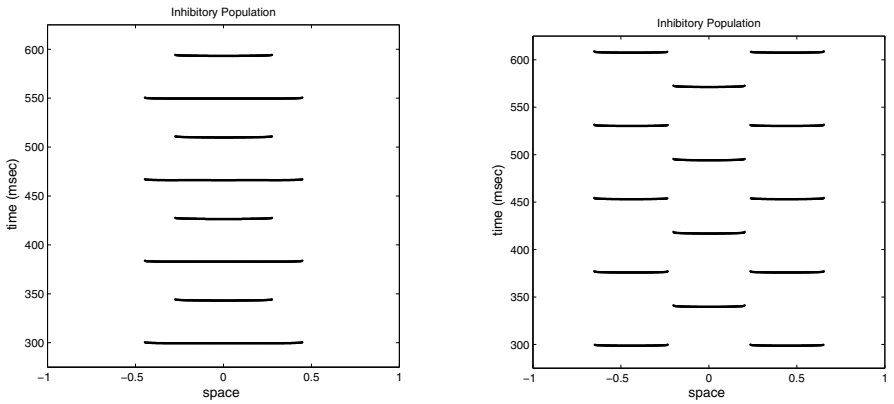

(a) $\sigma_i = 1.0$. (b) $\sigma_i = 1.234$.

Figure 2. *Other spatial patterns generated in the inhibitory model.* (a) *An example of a common type of spatial pattern characterized by the alternating widths of an interval of spiking cells firing nearly synchronous action potentials. Such solutions are characteristic of a period* 2 *orbit for a discrete map that describes the cycle-to-cycle variation in the width of the band of spiking cells.* (b) *Other spatial patterns arise which exhibit intervals of synchronously firing cells separated by gaps of neurons that fire on alternate cycles. One such example occurs when the spatial extent of the input* σ_i *is increased. Other parameters are* $g_{ii}^c = 5.0$, $I_i^c = 1.0$, $\sigma_{ii}^c = 1.0$.

2.3. Synchronous oscillations in the excitatory-inhibitory model. With strong inhibition and sufficiently weak excitation, numerical simulations of (2.1) for the excitatory-inhibitory population similarly exhibit a single continuous band of synchronously spiking neurons. These are localized examples of either ING or PING mechanisms [28, 5]. Analogous to the inhibitory network, the widths of the spiking band in both populations were commonly found to approach either a constant width or an alternation between two widths. Figure 3 shows two such examples of this behavior that we wish to capture qualitatively in a two-dimensional discrete map. In some cases, the bifurcation to the alternating widths appears supercritical, whereas in others it appears subcritical with a sharp transition to an alternation between significantly different widths. The excitatory synaptic currents arise from AMPA receptors (a subset of receptors for the transmitter glutamate) and have a time constant of decay $\beta_e^{-1} \approx 1$–2 ms. However, these currents decay well before the end of the gamma oscillation period. In section 4, we additionally consider a longer time constant to extend the effect of excitation to the end of the gamma cycle, motivated by results of the associated discrete map. NMDA receptor-mediated excitatory synaptic currents (another glutamate circuit) are a common example in the brain with a substantially longer time constant.

3. Heuristic map for the inhibitory network. In this section, we motivate and analyze a one-dimensional discrete map that serves as a qualitative description for the spatial extent of the localized band of synchronous oscillations described in section 2.2. With inhibition serving as the organizing force for synchronized oscillations, the idea is to collapse the spatially coherent oscillations onto the iterates of a discrete map that describes the evolution of the width of the localized band of synchronously firing neurons which is assumed to evolve symmetrically about the input. The map qualitatively reflects the behavior of the full spatially

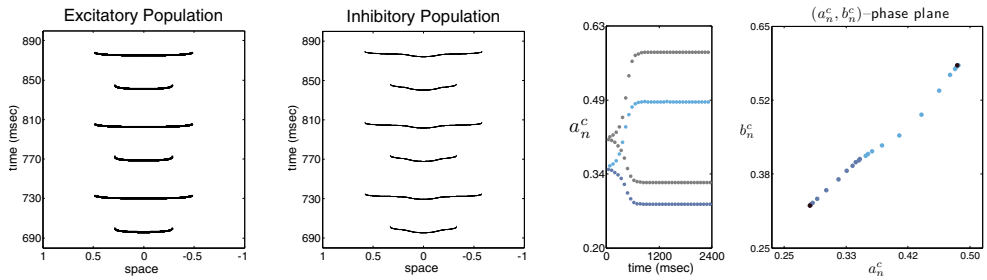

(a) $g_{ie}^c = 2.0$—alternating width solution.

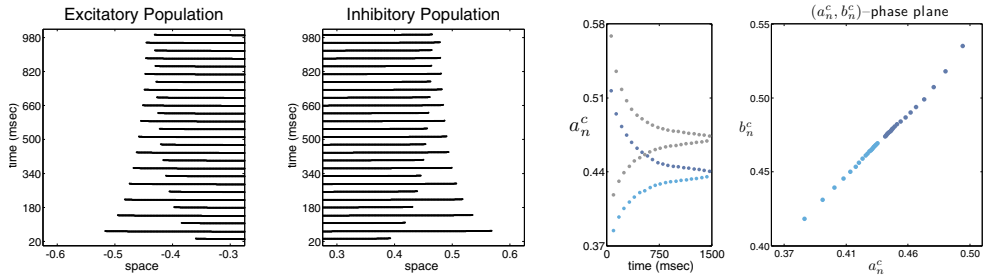

(b) $g_{ie}^c = 2.1$—transient approach near the bifurcation point.

Figure 3. *Synchronous oscillations in the excitatory-inhibitory conductance-based model. In each row, the first two figures are rastergrams illustrating the synchronous band of action potentials in each population; the third plot depicts the evolution of the halfwidth a_n^c of the band of spikes in the excitatory population (blues) and the halfwidth b_n^c in the inhibitory population (gray), respectively; and the last figure is the corresponding orbit in the (a_n^c, b_n^c) plane with every second iterate colored identically to highlight that the conductance-based model exhibits the suborbit behavior of a discrete map.* (a) *A periodic spatial pattern in the form of a single band of synchronously spiking neurons, whose width alternates cycle-by-cycle, resembling a stable period* 2 *orbit in a discrete map.* (b) *Approach of the transient near the flip bifurcation point. Common parameters:* $I_e^c = I_i^c = \sigma_e^c = 1$, $\sigma_i^c = 0.5$, $g_{ee}^c = 1$, $g_{ei} = 2.12$, $g_{ii}^c = 2$, $\sigma_{ee}^c = \sigma_{ei}^c = \sigma_{ie}^c = \sigma_{ii}^c = 1$, $\beta_e = 0.5$, *and parameters in Appendix* A.

extended system, exhibiting stable fixed points and period 2 orbits. A fixed point represents a fixed interval of neurons that fire on every cycle, with the remainder of the population quiescent. A period 2 orbit represents a periodic alternation of a larger interval followed by a shorter interval of synchronously firing neurons. We derive existence and stability conditions for fixed points of the one-dimensional map and demonstrate that, under our assumptions, a fixed point loses stability only in a flip bifurcation. Subsequently, in section 3.2 we attempt a more systematic approach to determining how the parameter values of the map relate to the conductance-based model. In section 3.3, we include and analyze an additional term that incorporates the effect of early-cycle inhibition on the width of the pulse. Finally, in section 3.4 we analyze the case where the left and right boundaries of the band of oscillations are allowed to evolve independently, and find that the symmetric-boundary and dual-boundary formulations result in equivalent stability conditions for fixed points.

3.1. One-dimensional discrete map for an inhibitory cell population. As in section 2.2, we assume that the inhibitory population is stimulated by a localized, even-symmetric, Gaussian-like input $I(x)$ and that the activity of the network is mediated by distance-dependent

inhibitory synaptic coupling. In particular, we assume that this combination results in a band (interval) of cells, localized about the input, that fires nearly synchronously as inhibition wanes at the end of each gamma cycle. Ignoring adaptation and other nontrivial currents, this assumption is reasonable given that the refractory period of neurons is much shorter than the period of the gamma oscillation, which is set by the time course of the decay of synaptic inhibition.

Assumptions and heuristics. We now cast the network in a continuum formulation that is commensurate with system (2.1) in which x is a continuous variable and the sums become spatial integrals over the spiking region. A *continuum model* for an inhibitory population as described in section 2.2 is given by

$$C\frac{\partial v_i}{\partial t}(x,t) = -I^{\mathsf{ion}}(v_i, m_i, n_i, h_i) - I^{\mathsf{syn}}(x,t) + I^{\mathsf{input}}(x), \tag{3.1}$$

$$\tau_{q_i}(v_i)\frac{dq_i}{dt}(x,t) = q_i^{\infty}\big(v_i(x,t)\big) - q_i(x,t), \qquad q \in \{m_i, h_i, n_i\},$$

where the inhibitory synaptic current evolves according to

$$I^{\mathsf{syn}}(x,t) = g_{ii}^{c}\int_{\mathbb{R}} w_{ii}(x-y)\, s_i(y,t)\Big[v_i(x,t) - V_i^{\mathsf{syn}}\Big]\, dy,$$

$$\frac{ds_i}{dt}(x,t) = \alpha_i\kappa\big(v_i(x,t)\big)(1 - s_i(x,t)) - \beta_i s_i(x,t).$$

We take system (3.1) to be defined on the infinite domain with boundary conditions requiring all variables to approach equilibrium values as $x \to \pm\infty$. We assume that the mix of the localized (excitatory) input current and the resultant inhibitory current generates a single continuous band of nearly synchronous action potentials.

Since the symmetric input decays with distance from its center, we assume for simplicity that the band of activity evolves symmetrically about the input (however, see section 3.4). The halfwidth b_n defines the symmetric distance from the center of the input to the boundaries of the band $(-b_n, b_n)$ of neurons firing at the start of the nth gamma cycle, with all other cells quiescent. For each cycle n, a nonempty interval $(-b_n, b_n)$ of cells fires synchronously, generating inhibitory currents seen by all cells over the duration of the cycle. We compose the inhibitory synaptic current density $\tilde{g}_{\mathsf{syn}}(x,y,t)$, from the cell at y to the cell at x, as the product of a synaptic current amplitude $\bar{g}_{ii}$, a uniform synaptic conductance time course $S_{\mathsf{syn}}(t)$, and a distance-dependent weight function w_{ii}, which is positive and normalized to 1 over $\mathbb{R}$; i.e.,

$$\tilde{g}_{\mathsf{syn}}(x,y,t) \;=\; \bar{g}_{ii}\, w_{ii}(x-y)\, S(y,t),$$

where $S(y,t) = S_{\mathsf{syn}}(t)$ for any $y \in (-b_n, b_n)$, with $S(y,t) = 0$ otherwise, to produce synaptic currents only from cells firing action potentials. Though g_{ii}^{c} in section 2.1 represents a synaptic conductance, as a simplification we effectively subsume the conductance amplitude and reversal potential to interpret $\bar{g}_{ii}$ as a synaptic *current* amplitude.

To relate how the currents initiated on the nth cycle determine the halfwidth b_{n+1} of cells firing on the next cycle, we make the following set of simplifying assumptions. As motivating these assumptions becomes somewhat involved, we state the assumptions and refer the reader to section 3.2 where they are examined in more detail.

(1) We assume that the gamma oscillation is exactly periodic; i.e., since $b_n > 0$ for all n, the cycle length T_n, which is the time between any two consecutive spikes, measured using the centers of the intervals $(-b_n, b_n)$ and $(-b_{n+1}, b_{n+1})$, is the same from cycle to cycle so that $T_n = T$ for all $n > 0$.

(2) Any synaptic current present during a cycle is the result only of neurons firing at the beginning of that cycle and is reset to zero at the end of the cycle.

(3) A cell fires a spike at the end of the cycle if the instantaneous total current entering the cell has exceeded a hard threshold θ_i.

(4) We neglect any edge effects that result from boundary layers in the evolution of the gating variables of the spiking currents associated with thresholding.

Assuming the existence of a single, bounded, continuous band of spiking cells, we define the total time-dependent synaptic current $\tilde{G}_{ii,n}(x,t)$ to the cell at x from only cells that fired on cycle n (with $t = 0$ corresponding to the beginning of cycle n). Since the synaptic currents are generated only by the cells in the interval $(-b_n, b_n)$,

$$\tilde{G}_{ii,n}(x,t) \;=\; \int_{\mathbb{R}} \bar{g}_{ii}\, w_{ii}(x-y)\, S(y,t)\, dy \;=\; \bar{g}_{ii}\, S_{\mathsf{syn}}(t) \int_{-b_n}^{b_n} w_{ii}(x-y)\, dy.$$

Corresponding to the end of cycle n, we set $t = T$ and define the synaptic current amplitude at the threshold event:

$$g_{ii} \;=\; \bar{g}_{ii}\, S_{\mathsf{syn}}(T).$$

The total synaptic current to the cell at x from the band $(-b_n, b_n)$ of neurons is, thus,

$$J_{ii}\,(x, b_n) \;=\; g_{ii} \int_{-b_n}^{b_n} w_{ii}(x-y)\, dy. \tag{3.2}$$

The convention is for the first variable x to be associated with postsynaptic cells and the second variable b_n to be associated with presynaptic cells, so that $J_{ii}(x, b_n)$ represents the total (instantaneous) synaptic current *from* the interval of spiking cells $(-b_n, b_n)$ at the beginning of the cycle *to* the cell at location x at the end of the nth cycle. Thus, the total current I_n^{tot} to the cell at x at the end of the nth cycle is given by

$$I_n^{\mathrm{tot}}(x) \;=\; I(x) - J_{ii}\,(x, b_n).$$

Note that we take $g_{ii} > 0$ and subtract the current J_{ii} to represent synaptic inhibition. As before, the input $I(x)$ and synaptic weight $w_{ii}(x)$ are taken to be even-symmetric, Gaussian-like, $\mathcal{C}^1$ functions that monotonically decay to 0 as $x \to \pm\infty$. We define I_i and σ_i to represent the input current amplitude and its spatial extent and consider only excitatory inputs $I_i > 0$. For simulations, we use $I(x) = I_i\, e^{-(x/\sigma_i)^2}$ and

$$w_{ii}(x) = \frac{1}{\sqrt{\pi}\sigma_{ii}} e^{-\left(\frac{x^2}{\sigma_{ii}^2}\right)} \quad\Longrightarrow\quad J_{ii}(x,y) = \frac{g_{ii}}{2}\left[\operatorname{erf}\left(\frac{x+y}{\sigma_{ii}}\right) - \operatorname{erf}\left(\frac{x-y}{\sigma_{ii}}\right)\right]. \tag{3.3}$$

Implicit map for an inhibitory population. The cell at x fires an action potential if the total current $I_n^{\text{tot}}(x)$ to that cell exceeds the current threshold θ_i before the end of the cycle. For a single, superthreshold interval $(-b_{n+1}, b_{n+1})$ of neurons to fire a spike at the beginning of the $(n+1)$th cycle, it follows that, by the end of the nth cycle, the total current to any cell $x \in (-b_{n+1}, b_{n+1})$ must be above the threshold current θ_i and be subthreshold for x otherwise. The symmetric boundaries $x = \pm b_{n+1}$ correspond to the threshold current for firing, i.e.,

$$\theta_i \;=\; I(b_{n+1}) - J_{ii}\,(b_{n+1}, b_n).$$

Therefore, defining the nonlinear function

$$F(b_n, b_{n+1}) \;=\; I(b_{n+1}) \;-\; J_{ii}\,(b_{n+1}, b_n) \;-\; \theta_i,$$

the *inhibitory map* is given by the one-dimensional implicit discrete map

$$F(b_n, b_{n+1}) = 0, \tag{3.4}$$

which determines, implicitly, the halfwidth b_{n+1} of the band of spiking cells on the $(n+1)$th cycle as a result of the input and the synaptic currents generated by the band of neurons with halfwidth b_n on the nth cycle. Since the boundaries are assumed to evolve symmetrically, we consider only $b_n, b_{n+1} > 0$.

A few immediate issues arise in the implicit formulation of the map: (1) given an initial value, it is not guaranteed that a solution exists; (2) the dynamical system may not be well-defined, as the map may not guarantee a unique solution at every iteration; and (3) each iteration of the map requires solving the nonlinear equation numerically. There are, indeed, cases in which a first iterate does not exist and also cases where a subsequent iterate fails to exist after a finite number of iterates. Typically, when a solution does exists for (3.4), it is single-valued and well-defined, provided that σ_i is not too large. In some cases, it might be appropriate to assign a *zero-width* solution $b_{n+1} = 0$. For example, if $F(b_n, b_{n+1}) < 0$ for $b_{n+1} > 0$, which yields no solution, the interpretation could be that the input is insufficient to excite *any* region of cells. If $b_{n+1} = 0$, the network is free of inhibition, and the input I and threshold θ_i alone determine b_{n+2}. Cyclic behavior typically ensues, effectively skipping cycles, and such behavior was occasionally seen in the conductance-based model. The zero solution is merely a way of continuing the solution in the map which concerns only the evolution of a single continuous band; alternately, one could expect a transition to more complex spatial patterns in the conductance-based model in which the continuous band breaks into excited regions separated by gaps.

Linear stability. We consider the evolution of an arbitrary small perturbation φ_n of a fixed point $\bar{b}$ of the implicit nonlinear map $F(b_n, b_{n+1}) = 0$. Setting

$$b_n = \bar{b} + \varphi_n$$

and expanding F in a Taylor series,

$$F(\bar{b} + \varphi_n, \bar{b} + \varphi_{n+1}) \;=\; F(\bar{b}, \bar{b}) \;+\; D_1 F\big(\bar{b}, \bar{b}\big)\,\varphi_n \;+\; D_2 F\big(\bar{b}, \bar{b}\big)\,\varphi_{n+1} \;+\; \cdots,$$

the perturbations, to first order in φ_n, φ_{n+1}, satisfy

$$D_1F(\bar{b},\bar{b})\,\varphi_n \;+\; D_2F(\bar{b},\bar{b})\,\varphi_{n+1} \;=\; 0.$$

Assuming $D_2F(\bar{b},\bar{b}) \neq 0$, we obtain the linearized map about the fixed point $\bar{b}$,

$$\varphi_{n+1} \;=\; \Lambda\big(\bar{b}\big)\,\varphi_n,$$

where

$$\Lambda\big(\bar{b}\big) \;=\; -\frac{D_1F(\bar{b},\bar{b})}{D_2F(\bar{b},\bar{b})} \;=\; \frac{D_2J_{ii}(\bar{b},\bar{b})}{I_i'(\bar{b}) - D_1J_{ii}(\bar{b},\bar{b})}. \tag{3.5}$$

The usual condition for asymptotic stability of the fixed point $\bar{b}$ is

$$\big|\Lambda\big(\bar{b}\big)\big| \;<\; 1. \tag{3.6}$$

To proceed further, we calculate the following derivatives:

$$\begin{aligned}
D_1J_{ii}(x,y) \;&=\; g_{ii}\cdot\frac{\partial}{\partial x}\int_{-y}^{y} w_{ii}(x-\xi)\,d\xi \;=\; -g_{ii}\Big(w_{ii}(x-y) - w_{ii}(x+y)\Big),\\
D_2J_{ii}(x,y) \;&=\; g_{ii}\cdot\frac{\partial}{\partial y}\int_{-y}^{y} w_{ii}(x-\xi)\,d\xi \;=\; +g_{ii}\Big(w_{ii}(x-y) + w_{ii}(x+y)\Big).
\end{aligned}$$

Using the even symmetry of w_{ii}, we find

$$\begin{aligned}
D_1F(x,y) \;&=\; -D_2J_{ii}(y,x) \;=\; -g_{ii}\Big(w_{ii}(x-y) + w_{ii}(x+y)\Big),\\
D_2F(x,y) \;&=\; -D_1J_{ii}(y,x) + I'(y) \;=\; g_{ii}\Big(w_{ii}(x-y) - w_{ii}(x+y)\Big) + I'(y),
\end{aligned} \tag{3.7}$$

which yields

$$\Lambda\big(\bar{b}\big) \;=\; \frac{g_{ii}\left(w_{ii}\big(0\big) + w_{ii}\big(2\bar{b}\big)\right)}{g_{ii}\left(w_{ii}\big(0\big) - w_{ii}\big(2\bar{b}\big)\right) + I'\big(\bar{b}\big)}.$$

For any fixed point $\bar{b}$ such that $\Lambda(\bar{b}) > 0$, condition (3.6) implies

$$1 < \frac{1}{\Lambda} \;=\; \frac{g_{ii}\left(w_{ii}\big(0\big) - w_{ii}\big(2\bar{b}\big)\right) + I'\big(\bar{b}\big)}{g_{ii}\left(w_{ii}\big(0\big) + w_{ii}\big(2\bar{b}\big)\right)}.$$

By inspection, this condition is never satisfied under our assumptions that $w_{ii}(x) > 0$, $w_{ii}'(x) < 0$, and $I'(x) < 0$, for $x > 0$, and any such fixed points are, therefore, unstable.

Stable fixed points are possible only if $\Lambda(\bar{b}) < 0$, in which case condition (3.6) becomes

$$-1 > \frac{1}{\Lambda} \;=\; \frac{g_{ii}\left(w_{ii}\big(0\big) - w_{ii}\big(2\bar{b}\big)\right) + I'\big(\bar{b}\big)}{g_{ii}\left(w_{ii}\big(0\big) + w_{ii}\big(2\bar{b}\big)\right)}.$$

The expression in the denominator is positive, and the stability condition reduces to

$$I'(\bar{b}) \;<\; -2\,g_{ii}\,w_{ii}(0). \tag{3.8}$$

Since $I'(\bar{b}) < 0$ for any fixed point $\bar{b}$, this condition indicates that the gradient of the input at the boundary point must be sufficiently steep for a fixed point to be stable.

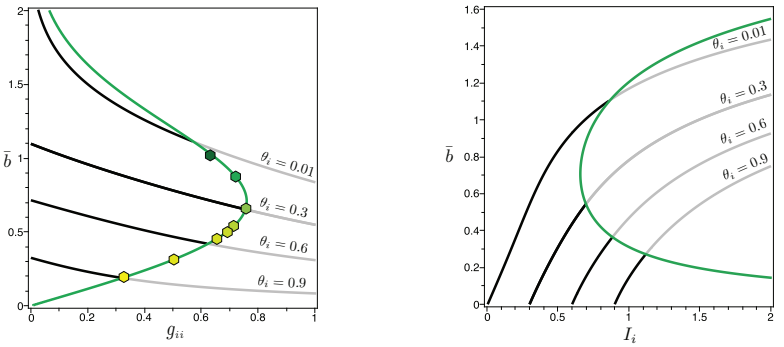

(a) Fixed $I_i = 1.0$. (b) Fixed $g_{ii} = 0.5$.

Figure 4. *Bifurcation diagrams: dependence of the fixed point* $\bar{b}$ (a) *on* g_{ii} *and* (b) *on* I_i*, for various fixed values of* θ_i*. Black (gray) curves correspond to stable (unstable) fixed points. Intersection points with the green curve correspond to flip bifurcation points of the fixed point. Other parameters are* $\sigma_i = 1$, $\sigma_{ii} = 1$*. Varying* σ_i *or* σ_{ii} *produces qualitatively similar diagrams, though the bifurcation curves for each* θ_i *intersect the curve of flip bifurcations in different locations.*

Fixed point loses stability through a flip bifurcation only. We expect a flip bifurcation of a fixed point to occur when the fixed point $\bar{b} = \bar{b}^*$ satisfies

$$\Lambda(\bar{b}^*) = -1 \qquad \Longrightarrow \qquad D_1 F(\bar{b}^*, \bar{b}^*) = D_2 F(\bar{b}^*, \bar{b}^*),$$

which reduces to

$$I'(\bar{b}^*) = -2\, g_{ii}\, w_{ii}(0). \tag{3.9}$$

Therefore, from (3.8) any stable fixed point $\bar{b}$ of the inhibitory map (3.4) can lose stability only through a flip bifurcation under the above assumptions on w_{ii} and I.

Bifurcation diagrams. The eigenvalue $\Lambda(\bar{b})$ may be calculated for the Gaussian input and synaptic weight functions (3.3) using (3.7). In this case, the fixed point $\bar{b}$ is stable if

$$\sqrt{\pi}\, \frac{I_i\, \sigma_{ii}}{g_{ii}\, \sigma_i^2}\, \bar{b}\, e^{-\frac{\bar{b}^2}{\sigma_i^2}} > 1$$

with a flip bifurcation occurring at equality. The equation $F(\bar{b}, \bar{b}) = 0$ is solved numerically to determine the dependence of the fixed point $\bar{b}$ on other parameters. Without loss of generality, we set the space scale by taking $\sigma_{ii} = 1$. In Figure 4, bifurcation diagrams show how, for fixed θ_i, the fixed point varies with respect to either g_{ii} or I_i in the case of Gaussian weight and input functions (3.3). If a fixed point $\bar{b}$ is stable for sufficiently small values of each of the parameters g_{ii}, I_i, σ_i, the fixed point loses stability in a flip bifurcation by increasing any variable while keeping all other variables fixed. This can be seen in stability condition (3.8)–(3.9). By inspection, for sufficiently small g_{ii}, the fixed point is stable. Increasing g_{ii}, keeping all other parameters fixed, results in a decrease in $\bar{b}$. If $I'(\bar{b})$ is bounded, then for sufficiently large g_{ii} inequality (3.8) fails to be satisfied, resulting in the loss of stability of

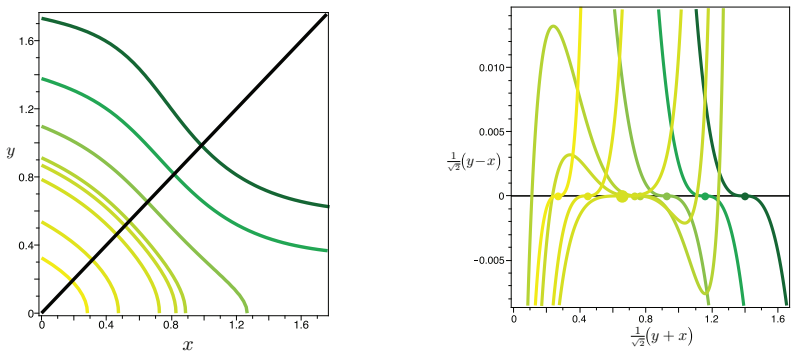

(a) Graph: $F(x, y) = 0$. (b) Graph: composition map.

Figure 5. (a) *The graph of the map* $F(x, y) = 0$ *at points along the curve of flip bifurcations (green curve) shown in Figure* 4(a) *for various fixed values of* $\theta_i \in (0.05, 0.9)$. (b) *The corresponding graphs for the composition map generated by* $F(x, y) = 0$*, which have been rotated through the angle* $-\frac{\pi}{4}$ *so that the line* $y = x$ *corresponds to the horizontal axis. This sequence of graphs reveals the structure of a generalized flip bifurcation with its codimension* 2 *point (large filled circle).*

the fixed point in a flip bifurcation. Although it appears that increasing I_i in inequality (3.8) should move the stable fixed point away from the flip bifurcation point, increasing I_i results in an increase in the halfwidth $\bar{b}$, keeping all other parameters constant. Since $I'(\bar{b}) \longrightarrow 0$ as $\bar{b} \longrightarrow \infty$, then, for sufficiently large I_i and $\bar{b}$, $I'(\bar{b})$ becomes sufficiently small that condition (3.8) fails. Thus, increasing I_i, keeping all other parameters fixed, destabilizes a fixed point though a flip bifurcation. This is similar for increasing σ_i since, if $I'(\bar{b})$ is bounded, increasing σ_i sufficiently will cause inequality (3.8) to fail. However, decreasing σ_i sufficiently has a similar effect since, by assumption, $I'(\bar{b}) \longrightarrow 0$ as $\bar{b} \longrightarrow \infty$. Thus a fixed point can lose stability in a flip bifurcation if σ_i is increased or decreased sufficiently.

Numerical simulations of the inhibitory map. Numerical simulations indicate that both supercritical and subcritical flip bifurcations occur. The direction of bifurcation was studied numerically by examining the evolution of the map from initial conditions that were small perturbations of the fixed point. The bifurcation was determined numerically to be supercritical if the iterates approached a period 2 orbit whose periodic points were very close to the equilibrium for parameter values just beyond the predicted bifurcation point. In some regions, the period 2 orbit persisted until the smaller of the periodic points approached 0, where the map breaks down. Further bifurcation to period 4 orbits was not seen. In other regions, the period 2 orbit appeared to vanish in a fold bifurcation with an ambient unstable period 2 orbit that could be detected prior to the bifurcation. Subcritical bifurcations typically exhibited a catastrophic loss of stability beyond the bifurcation point, with small perturbations of the fixed point leading to exponentially diverging iterates alternating between two positive values about the fixed point, with one rapidly approaching 0. These numerics are consistent with the signature of the generalized flip bifurcation present in the graphs of the composition map in Figure 5(b), which are sampled along the curve of flip bifurcations in Figure 4(a). Once iterates of the map approach 0, the map breaks down at an iterate for which no positive solution exists. In order to continue the solution at such an iterate, it is possible to redefine the map

in a piecewise manner so that, if no solution to $F(b_n, b_{n+1}) = 0$ exists, we interpret this as the *zero solution* (no neurons fire) and take $b_{n+1} = 0$. Subsequently, the solution essentially becomes a period 2 orbit, alternating between 0 and a positive value.

3.2. Comparison with the associated conductance-based model. We begin our comparison by identifying the relationships between the parameters of the inhibitory map (3.4) and their counterparts in the corresponding conductance-based model (2.1). Some are straightforward, but others are more complicated and highlight some of the issues regarding assumptions (1)–(4) in section 3.1. Although it is not conducive to predicting the precise width, the inhibitory map nonetheless is capable of predicting moderately close values for the width of the band, and, moreover, does share many qualitative features with the conductance-based model. We also demonstrate that inhibition on two time scales ultimately determines the width of the pulse, suggesting a modification to the inhibitory map that is briefly explored in section 3.3.

It is natural to take the amplitude of the input I_i, its characteristic width σ_i, and the characteristic width σ_{ii} of the inhibitory synaptic connections to be identical to those in the conductance-based model, namely, I_i^c, σ_i^c, and σ_{ii}^c, respectively. However, the threshold θ_i and the inhibitory conductance parameter g_{ii} in the inhibitory map form more complicated relationships with parameters in the conductance-based model. The threshold θ_i can be taken to reflect the oscillation frequency of the synchronous action potentials in the following sense. Equations (3.4) for the inhibitory map determine at which points in the space the total sum of excitatory and inhibitory currents is above the threshold for firing by the end of each cycle. Although the threshold in the conductance-based model is dynamic, as a first approximation we can interpret θ_i as equal to the constant current I_i^c necessary, based upon the FI-curve, for the model neuron to fire repetitive action potentials at the frequency of the synchronous oscillations. That is, it serves as an approximation for the minimum current necessary to fire an action potential before the end of the cycle when the wave of inhibition prevents spiking. Even this approximation creates an inherent difficulty in closing the dependence of θ_i on the other parameters of the map. We do not attempt to ascertain such a relationship in this treatment and simply use the FI-curve to determine θ_i from the frequency of oscillation in the conductance-based model.

There are intuitive relationships between θ_i and the parameters g_{ii}^c, I_i^c, and σ_i^c in the conductance-based model (indicated by superscript ^{c}). Increasing g_{ii}^c increases the strength of inhibition, which tends to slow down the oscillation, implying that θ_i should decrease. Increasing I_i^c enables the cells to fire more rapidly, implying that θ_i should increase. The map essentially captures whether or not a cell fires in the parameters θ_i and g_{ii}. If θ_i represents the current necessary to produce firing at the oscillation frequency of the network, then g_{ii} effectively determines the rest. The lack of a strict threshold makes it difficult to express the threshold condition perfectly. As a lowest order approximation, we assumed in section 3.1 that, at the end of each cycle, any cell whose input current was above threshold θ_i necessarily fired an action potential.

In (3.2) of the derivation of the inhibitory map, we assumed

$$g_{ii} \;=\; \bar{g}_{ii}\, S_{\mathsf{syn}}(T),$$

where S is the synaptic time course, T the period of the oscillation, and $\bar{g}_{ii}$ a constant to

be determined. For comparison, in the conductance-based model the instantaneous current input, at the end of the cycle ($t = T$), from another cell is

$$-g_{ii}^c\, s_{ii}(T)\left[v(T) - V_i^{\mathsf{syn}}\right],$$

where $v(T)$ is the membrane potential of the postsynaptic cell sampled at the end of the cycle, V_i^{syn} is the reversal potential for GABA_A receptors which mediate the inhibitory synaptic current, and $s_{ii}(T) \in [0,1]$ is the synaptic gating variable sampled at the end of the cycle. This suggests the following relationships:

$$\bar{g}_{ii} = -g_{ii}^c\left(v(T) - V_i^{\mathsf{syn}}\right), \qquad s_{ii}(T) = S_{\mathsf{syn}}(T).$$

The synaptic gating variable s_{ii} evolves according to a differential equation, and consequently the synaptic time course is actually dependent on the dynamics. However, given that the period of the oscillation is long, we can approximate the synapses simply by exponential decay so that at the end of the cycle

$$S_{\mathsf{syn}}(T) = e^{-\left(\frac{T}{\tau_{\mathrm{GABA}_A}}\right)}.$$

Since $\beta_i = 0.1$ ms for the inhibitory synaptic kinetics of the conductance-based model (parameters in Appendix A), we take $\tau_{\mathrm{GABA}_A} = 10$ ms. During transients in the conductance-based model, the value of T changes cycle-by-cycle; if the solution is a fixed point, then T is constant cycle-by-cycle. Although this suggests that the map is best suited for fixed point solutions because T is assumed to be constant, it nonetheless serves as a lowest order approximation for transients and period 2 orbits since the variations in cycle length are generally small.

To determine g_{ii}^c, we consider $v_i(x,t)$ around the threshold event at the end of the cycle. For $x < b_n$, threshold is crossed and a spike generated. At $x = b_n$, the voltage trace $v_i(b_n,t)$ achieves a subthreshold maximum and then decreases to more negative values. This turning point between firing and not firing serves as an estimate for the critical voltage $v(T)$ associated with the threshold event. In the conductance-based model, with the parameters given in Appendix A, the corresponding membrane potential $v_i(b_n,T)$ often lies in the range $[-60,-50]$. As the dependence is difficult to ascertain, for simplicity we can use a single approximation for all parameter values, e.g., $v_i(b_n,T) = -56$ mV. Regardless of how $v(T)$ is chosen, we obtain the relation

$$g_{ii} = \bar{g}_{ii}\, S_{\mathsf{syn}}(T) = g_{ii}^c\, e^{-\left(\frac{T}{\tau_{\mathrm{GABA}_A}}\right)}\left[v(T) - V_i^{\mathsf{syn}}\right].$$

Although the map does not determine the precise value of the width of the spiking region in the case of a fixed point, the predicted value can be reasonably close. For example, choosing $g_{ii}^c = 5$, $I_i^c = 1$, $\sigma_i^c = 0.5$, $\sigma_{ii}^c = 1$ in the conductance-based model results in a solution alternating between widths of 0.147 and 0.1485 with an approximate frequency of 29.3 Hz and period $T = 34.1$ ms. Taking $v(b_n,T) = -56$ mV, the parameters for the map are given as $I_i = 1$, $\sigma_i = 0.5$, $\sigma_{ii} = 1$, $g_{ii} = 3.139$, $\theta_i = 0.24$, in which case the corresponding fixed point in the map is $\bar{b} = 0.186$.

The prediction from the map, in a sense, is an upper bound, assuming that all cells fire exactly synchronously and do not feel the effects of the ensuing wave of inhibition. However,

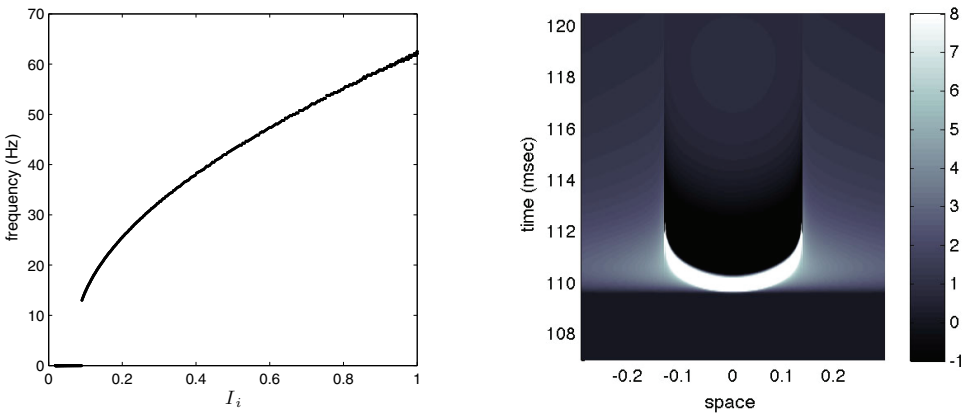

(a) FI-curve for the conductance-based model. (b) Early-cycle inhibitory synaptic current.

Figure 6. (a) *FI-curve for the single-neuron version of the conductance-based model* (2.1) *with parameters given in Appendix* A*, which relates the steady-state firing frequency of periodic action potentials in an individual neuron (spatial point) as a function of the amplitude of the constant input current* I_i^c*. This curve can be used as an approximation of the threshold current* θ_i *for firing in the inhibitory map* (3.4). (b) *Inhibitory synaptic current* $-I^{\text{syn}}(x,t)$ *as a function of space and time. Space is in units of the synaptic space constant* σ_{ii}*. The bright white region indicates the large deviation from the* $GABA_A$ *reversal potential during the action potential.*

as mentioned previously, the cells do not fire in perfect synchrony due to the spatial variation of input and synaptic currents. Consequently, the region of spiking cells is expected to be smaller than that predicted by the map since the inhibition generated by cells firing early will inhibit latent cells in the periphery which are nearing threshold. Figure 6(b), which plots the inhibitory synaptic current I^{syn} as a function of time and space, illustrates the effect of the cells firing earliest, which subsequently inhibit those near the boundaries of the region of spiking cells. The white region represents large deviation from the GABA_A reversal potential V_i^{syn} for those cells firing an action potential, and inhibition is clearly present in the neighboring region. It is generally the case that the map predicts a larger region than is exhibited in the conductance-based model. Delaying the effects of the onset of inhibition by lengthening its time constant does produce a wider pulse. Alternatively, to reduce the latency between the firing of the first and last cells, one can use inputs of the form $I(x) = I_i^c e^{-(x/\sigma_i^c)^{2n}}$, $n \geq 2$, which are more steplike, to produce tighter synchrony.

We now turn to qualitative comparisons between the conductance-based model and the inhibitory map. Both models exhibit fixed point and period 2 orbit solutions for the width of the spiking band on each cycle. However, supercritical flip bifurcations appeared more commonly in the conductance-based model than in the map. This difference could be due to the assumption of a constant period of oscillation from cycle to cycle in the map, whereas in the conductance-based model there are two slightly different cycle lengths in the period 2 orbit. Although an exhaustive search was not performed, bifurcation to period 4 orbits was exhibited in neither the conductance-based model nor the map. Although small variation in the widths is seen in the conductance-based model, an orbit was determined to be a period N orbit if the widths were substantially different and periodic after a transient.

Further qualitative analysis is assessed in the vicinity of the flip bifurcation. In particular, we considered period 2 orbits with small differences in the alternating widths of the spiking region. Consistent with the bifurcation analysis of the inhibitory map, increasing I_i^c or σ_i^c in the conductance-based model moved the system away from the flip bifurcation, reflected in a larger difference in the alternating widths of the period 2 orbit. However, increasing g_{ii}^c is more subtle. In the conductance-based model, increasing g_{ii}^c was seen in some parameter regions to move the system closer to the bifurcation point, reflected by a smaller difference in the alternating widths of the period 2 orbit. In other regions of parameter space, it did not bring the system closer to the bifurcation point, in some cases leading to break-up of the continuous band. In Figure 4(a), if θ_i remains constant, then the inhibitory map suggests that increasing g_{ii}^c in the conductance-based model should move the system undergoing a flip bifurcation farther beyond the flip bifurcation point, thereby enlarging the difference between the two widths. However, increasing the strength of inhibition g_{ii}^c results in a decrease in oscillation frequency, indicating that θ_i must also decrease. Examining Figure 4(a), beyond the flip bifurcation curve where the fixed point is unstable, in some regions one can simultaneously increase g_{ii} and decrease θ_i to bring the map closer to the bifurcation point, whereas in other regions these changes do not have that effect. The former is particularly enhanced when considering the addition of a form of *early-cycle inhibition* to the inhibitory map (see Figure 7).

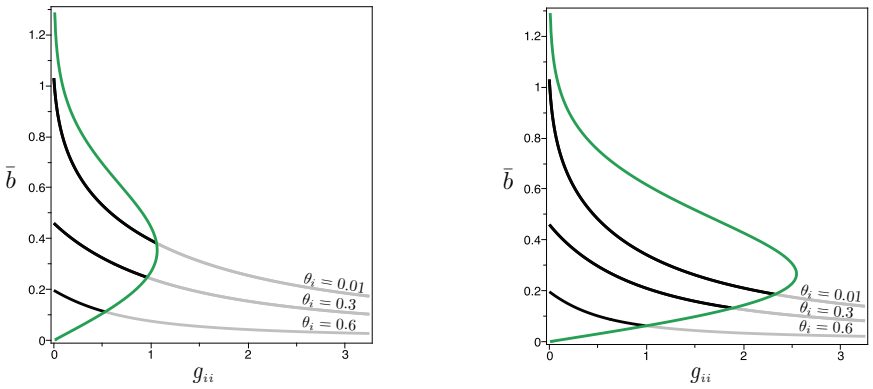

(a) Without early-cycle inhibition. (b) With early-cycle inhibition.

Figure 7. *Comparison of the stable and unstable fixed points and flip bifurcation points in the standard inhibitory map without* (3.4) *and with the early-cycle inhibition* (3.10). *Parameter values for* (a) $g_{ii}^* = 0.0$ *and for* (b) $g_{ii}^* = 0.7g_{ii}$, $\gamma = 0.4$. *Common to both cases:* $I_i = 0.7$, $\sigma_i = 0.5$.

3.3. Inhibitory map with early-cycle inhibition. Although in our model it has been assumed that the continuous interval of spiking cells must fire exactly synchronously, i.e., with zero lag from the first cells firing to the last, this perfect synchrony is not generic in the conductance-based model due to varying levels of the input current and synaptic inhibition at different points in space. We are effectively collapsing to a single instant the duration of time from the first neurons spiking to the last in each cycle (see Figure 6(b)). This early phase of the cycle, which is related to the onset time of the new wave of inhibition, occurs at the beginning of the $(n+1)$th cycle and is assumed to be short relative to the period of the cycle.

We collapse the early phase into a single instant and incorporate it implicitly as follows.

If $(-b_{n+1}, b_{n+1})$ is the interval of cells which ultimately fires on the $(n+1)$th cycle, then, for some fixed $\gamma \in (0,1)$, we assume that a subinterval $(-\gamma b_{n+1}, \gamma b_{n+1})$ will fire earlier and enhance the inhibition, thereby narrowing the width of the ultimate interval $(-b_{n+1}, b_{n+1})$ from what would have occurred otherwise. We model this inhibition by including the additional inhibitory term to the map

$$-J^*_{ii}(b_{n+1}, b_{n+1}),$$

where J_{ii} and J^*_{ii} differ only in their synaptic strength constants, g_{ii} and g^*_{ii}, respectively. This inhibitory term could represent the time-averaged inhibitory current over the firing period. The map determining the iterates b_n is now given by

$$F^*(b_n, b_{n+1}) = 0, \tag{3.10}$$

where

$$F^*(b_n, b_{n+1}) \;=\; I(b_{n+1}) - J_{ii}\,(b_{n+1}, b_n) - J^*_{ii}\,(b_{n+1}, \gamma b_{n+1}) - \theta_i.$$

Linear stability follows similarly as before, with the eigenvalue $\Lambda(\bar{b})$ becoming

$$\Lambda\big(\bar{b}\big) \;=\; -\frac{D_1 F(\bar{b},\bar{b})}{D_2 F(\bar{b},\bar{b})} \;=\; \frac{D_2 J_{ii}(\bar{b},\bar{b})}{\big[I_i(\bar{b}) - D_1 J_{ii}(\bar{b},\bar{b})\big] - \big[D_1 J^*_{ii}(\bar{b},\bar{b}) + D_2 J^*_{ii}(\bar{b},\bar{b})\big]}.$$

Comparing with (3.5), we see that the denominator has the additional term

$$D_1 J^*_{ii}(\bar{b},\bar{b}) + D_2 J^*_{ii}(\bar{b},\bar{b}) \;=\; 2g^*_{ii} w_{ii}\big((1+\gamma)\bar{b}\big) > 0 \qquad \text{for all } \bar{b} > 0.$$

Following arguments analogous to those used before, the condition for stability reduces to

$$I'(\bar{b}) \;<\; -2\,g_{ii}\,w_{ii}(0) \;+\; 2g^*_{ii}\,w_{ii}\big((1+\gamma)\,\bar{b}\big). \tag{3.11}$$

Comparing this new condition (3.11) with the previous stability condition (3.8), we see that, since $I'(\bar{b}) < 0$, the additional inhibitory term widens the region of stability of a fixed point, increasingly with respect to γ. This effect can be seen in Figure 7.

3.4. Dual-boundary inhibitory map. We briefly consider an inhibitory map in which the two boundaries of the band of synchronous oscillations are allowed to evolve independently rather than evolving with even symmetry as was assumed previously. Let $x = -b_n$ represent the location of the left boundary of the spiking region, and let $x = c_n$ represent the location of the right boundary on the nth cycle, where $b_n, c_n > 0$ are the distances to each boundary from the center of the stationary input. In this case the *dual-boundary inhibitory map* takes the form

$$\begin{aligned} 0 \;&=\; F_{\mathrm{L}}(b_n, c_n, b_{n+1}) \;\equiv\; I_i(b_{n+1}) \;-\; J^2_{ii}(-b_{n+1}, b_n, c_n) \;-\; \theta_i, \\ 0 \;&=\; F_{\mathrm{R}}(b_n, c_n, c_{n+1}) \;\equiv\; I_i(c_{n+1}) \;-\; J^2_{ii}(+c_{n+1}, b_n, c_n) \;-\; \theta_i, \end{aligned} \tag{3.12}$$

where

$$J^2_{ii}(\xi, b_n, c_n) \;=\; \int_{-b_n}^{c_n} w(\xi - y)\,dy.$$

The even symmetry of I_i and w_{ii} implies that a fixed point must also be symmetric about the input; i.e., $(b_n, c_n) = (\bar{b}, \bar{b})$ for all n, where $\bar{b}$ solves $F_{\mathrm{L,R}}(\bar{b}, \bar{b}, \bar{b}) = 0$.

Let ϕ_n, ψ_n be small perturbations of the fixed point $(\bar{b}, \bar{b})$, and set

$$b_n \;=\; \bar{b} + \varphi_n, \qquad c_n \;=\; \bar{b} + \psi_n.$$

Expanding the nonlinearities $F_{\mathrm{L}}, F_{\mathrm{R}}$ in a Taylor series about the fixed point $(\bar{b}, \bar{b})$, the perturbations to first order satisfy

$$\begin{aligned} D_1F_{\mathrm{L}}^*\,\varphi_n + D_2F_{\mathrm{L}}^*\,\psi_n + D_3F_{\mathrm{L}}^*\,\varphi_{n+1} \;&=\; 0,\\ D_1F_{\mathrm{R}}^*\,\varphi_n + D_2F_{\mathrm{R}}^*\,\psi_n + D_3F_{\mathrm{R}}^*\,\psi_{n+1} \;&=\; 0, \end{aligned}$$

where $D_jF_{\mathrm{L}}^* = D_jF_{\mathrm{L}}(\bar{b}, \bar{b}, \bar{b})$ and $D_jF_{\mathrm{R}}^* = D_jF_{\mathrm{R}}(\bar{b}, \bar{b}, \bar{b})$ for $j = 1, 2, 3$. Assuming $D_3F_{\mathrm{R}}^*, D_3F_{\mathrm{L}}^* \neq 0$ leads to the two-dimensional linearized map

$$\begin{pmatrix} \varphi_{n+1} \\ \psi_{n+1} \end{pmatrix} \;=\; M_2 \begin{pmatrix} \varphi_n \\ \psi_n \end{pmatrix}, \qquad M_2 \;=\; \begin{bmatrix} -\frac{D_1F_{\mathrm{L}}^*}{D_3F_{\mathrm{L}}^*} & -\frac{D_2F_{\mathrm{L}}^*}{D_3F_{\mathrm{L}}^*} \\ -\frac{D_1F_{\mathrm{R}}^*}{D_3F_{\mathrm{R}}^*} & -\frac{D_2F_{\mathrm{R}}^*}{D_3F_{\mathrm{R}}^*} \end{bmatrix},$$

where

$$\begin{aligned} D_1F_{\mathrm{L}}^* &= -D_2J_{ii}^2(-\bar{b}, \bar{b}, \bar{b}), & D_1F_{\mathrm{R}}^* &= -D_2J_{ii}^2(\bar{b}, \bar{b}, \bar{b}),\\ D_2F_{\mathrm{L}}^* &= -D_3J_{ii}^2(-\bar{b}, \bar{b}, \bar{b}), & D_2F_{\mathrm{R}}^* &= -D_3J_{ii}^2(\bar{b}, \bar{b}, \bar{b}),\\ D_3F_{\mathrm{L}}^* &= -D_1J_{ii}^2(-\bar{b}, \bar{b}, \bar{b}) + I_i'(-\bar{b}), & D_3F_{\mathrm{R}}^* &= -D_1J_{ii}^2(\bar{b}, \bar{b}, \bar{b}) + I_i'(\bar{b}) \end{aligned}$$

and

$$\begin{aligned} D_1J_{ii}^2(x, \xi, \eta) \;&=\; g_{ii} \cdot \frac{\partial}{\partial x} \int_{-\xi}^{\eta} w(x - y)\, dy \;=\; -g_{ii}\Big[w(x - \eta) - w(x + \xi)\Big],\\ D_2J_{ii}^2(x, \xi, \eta) \;&=\; g_{ii} \cdot \frac{\partial}{\partial \xi} \int_{-\xi}^{\eta} w(x - y)\, dy \;=\; -g_{ii}\, w(x + \xi),\\ D_3J_{ii}^2(x, \xi, \eta) \;&=\; g_{ii} \cdot \frac{\partial}{\partial \eta} \int_{-\xi}^{\eta} w(x - y)\, dy \;=\; +g_{ii}\, w(x - \eta). \end{aligned}$$

Due to the symmetries of I_i and w_{ii}, the matrix M_2 has the form

$$M_2 \;=\; \begin{bmatrix} \Delta & \Gamma \\ \Gamma & \Delta \end{bmatrix},$$

where

$$\Delta \;=\; \frac{g_{ii}\, w(0)}{g_{ii}\left[w(0) - w(2\bar{b})\right] + I'(\bar{b})}, \qquad \Gamma \;=\; \frac{-g_{ii}\, w(2\bar{b})}{g_{ii}\left[w(0) - w(2\bar{b})\right] + I'(\bar{b})}.$$

Consequently, the eigenvalues of M_2 are given by $\lambda_{\pm} = \Delta \pm \Gamma$, which results in

$$\lambda_{\pm} \;=\; \frac{g_{ii}\left[w(0) \pm w(2\bar{b})\right]}{g_{ii}\left[w(0) - w(2\bar{b})\right] + I'(\bar{b})}.$$

Stability of the fixed point $(\bar{b}, \bar{b})$ requires that $|\lambda_\pm| < 1$. We follow the same approach to this inequality as in section 3.1. First, the condition $|\lambda_+| < 1$ is identical to the stability condition (3.8) for the symmetric-boundary inhibitory map (3.4), which reduces to

$$I'(\bar{b}) \ < \ -2\, g_{ii}\, w_{ii}(0).$$

The other stability condition $|\lambda_-| < 1$ is new. From the assumptions on w_{ii} we have

$$0 < w_{ii}(0) - w_{ii}(2\bar{b}) < w_{ii}(0) + w_{ii}(2\bar{b}) \qquad \text{for all } \bar{b} > 0,$$

which implies that $|\lambda_-| < |\lambda_+|$ for all $\bar{b} > 0$. Hence, the stability condition $|\lambda_-| < 1$ for the fixed point $(\bar{b}, \bar{b})$ is superseded by the condition $|\lambda_+| < 1$ in the case of the dual-boundary inhibitory map under the assumptions on w_{ii} and I_i. Consequently, the condition for stability of a fixed point in the dual-boundary inhibitory map (3.12) is determined by stability with respect to symmetric perturbations and is equivalent to stability condition (3.8) in the symmetric-boundary inhibitory map (3.4).

4. Heuristic map for an excitatory-inhibitory (E-I) network. In this section, we explore the natural extension of the one-dimensional inhibitory map in section 3 to an excitatory-inhibitory pair of mutually coupled populations. In section 4.1, we develop and analyze the linear stability of an implicit two-dimensional discrete map for the excitatory-inhibitory network exhibiting the localized synchronous oscillations exemplified in the numerical results of section 2.3. In section 4.2, we describe various types of solutions and bifurcations explored in numerical solutions of the E-I map. In section 4.3, we make qualitative comparisons between the solutions of the E-I map and those of the corresponding conductance-based model, including a nontrivial result demonstrating dynamics on an invariant circle and weak resonances in the conductance-based model as predicted by the discrete map. Finally, in section 4.4, using numerical simulations and linear stability analysis of the E-I map, we demonstrate a particularly interesting bifurcation exhibited by the E-I map, in which the two periodic points of a period 2 orbit individually undergo 1:2 strong resonance bifurcations, ultimately giving rise to a pair of double homoclinic tangles that generates rich dynamic behavior.

4.1. Two-dimensional discrete map for an excitatory-inhibitory population. The E-I map is developed in the same heuristic fashion as the inhibitory map, using the continuum formulation (3.1) of the spatially extended network with the addition of a second population $v_e(x,t)$ that forms excitatory synaptic interactions with both populations. We use the subscripts e and i to identify variables associated with the excitatory and inhibitory populations, respectively. The network is stimulated by a constant excitatory input $\hat{I}_u(x) > 0$ to each population $u \in \{e, i\}$ that is even-symmetric and localized in space. Both inputs share a common center $x = 0$, though the amplitude I_u and characteristic spatial extent σ_u of the inputs may differ for each population u.

In the absence of an input, the network is assumed to be excitable rather than oscillatory, and, as a first approximation, we assume that the input drives each population such that a continuous, localized band of action potentials about the input fires exactly periodically with the same period T for both populations. The two populations are assumed to be synchronized, though a small phase difference ($\ll T$) between the firing of two populations during each cycle

is permissible; this typically occurs in numerical simulations of system (2.1) as spiking in the excitatory population is slightly advanced relative to the inhibitory population. Each cycle begins at the threshold crossing of the band of action potentials, and the map is derived by collapsing each cycle to an iterate of the map.

Synaptic interactions between the two populations are mediated through distance-dependent synaptic coupling $w_{uv}(x-y)$, and each population is coupled to itself as well as to the other population. The synaptic currents are defined in a fashion analogous to that in section 3.1; i.e., the total synaptic current *from* an interval $(-y, y)$ of spiking cells within population v *to* the neuron at location x in population u is defined as

$$J_{uv}(x,y) \;=\; g_{uv}\int_{-y}^{y} w_{uv}(x-\xi)\,d\xi. \tag{4.1}$$

The synaptic strengths g_{ue} for the excitatory synaptic currents are determined similarly, with the time constant and reversal potential chosen appropriately. We take $g_{uv} \geq 0$ in all cases and allow the sign of the term $\pm J_{uv}$ to determine whether the synaptic current is excitatory $(+)$ or inhibitory $(-)$. Again, the ordering convention for subscripts uv and arguments (x,y) of $J_{uv}(x,y)$ is that the *first* denotes the *postsynaptic* neuron and the *second* denotes the *presynaptic* neuron. Thus, $J_{ei}(x,b_n)$ is the total synaptic current from a continuous band of inhibitory neurons with halfwidth b_n on the nth cycle to an excitatory neuron at the location x which is sampled at the end of the cycle. It is implicitly assumed that the strengths of excitation and inhibition are such that a one-to-one correspondence between the oscillations is maintained.

E-I map. We assume that the boundaries of the band of synchronous action potentials evolve symmetrically about the common center of the inputs, with $a_n, b_n > 0$ representing the halfwidths of these intervals during the nth cycle in the excitatory and inhibitory populations, respectively. At the end of cycle n, the total current to the neuron at x in population u is given by the sum of the input and synaptic currents,

$$\hat{I}_u(x) + J_{ue}(x,a_n) - J_{ui}(x,b_n).$$

Define the threshold currents θ_e, θ_i as the minimum currents necessary for any neuron in the respective populations to fire by the end of each cycle (assuming a fixed period T and, e.g., using the FI-curve). For $u \in \{e,i\}$, we define the function

$$F_u(a_n,b_n,x) \;=\; \hat{I}_u(x) + J_{ue}(x,a_n) - J_{ui}(x,b_n) - \theta_u,$$

which is positive (negative) at points x in population u where the total current is above (below) the threshold current at the end of the cycle. The condition for a single interval $(-c_u, c_u)$ of neurons in population u to fire nearly synchronous action potentials on the $(n+1)$th cycle is then given by

$$F_u(a_n,b_n,x) > 0, \quad x \in [0,c_u), \quad \text{and} \quad F_u(a_n,b_n,x) < 0, \quad x \in (c_u,\infty),$$

with the boundary $c_u > 0$ of the band determined by the equation $F_u(a_n,b_n,c_u) = 0$.

The *E-I map* governing the evolution of the halfwidth pair (a_{n+1}, b_{n+1}) is consequently given by the implicit two-dimensional discrete map

$$F_e(a_n, b_n, a_{n+1}) = 0, \qquad F_i(a_n, b_n, b_{n+1}) = 0, \tag{4.2}$$

with the nonlinearities expressed as

$$\begin{aligned} F_e(a_n, b_n, a_{n+1}) &= \hat{I}_e(a_{n+1}) + J_{ee}(a_{n+1}, a_n) - J_{ei}(a_{n+1}, b_n) - \theta_e, \\ F_i(a_n, b_n, b_{n+1}) &= \hat{I}_i(b_{n+1}) + J_{ie}(b_{n+1}, a_n) - J_{ii}(b_{n+1}, b_n) - \theta_i. \end{aligned}$$

The equations for a_{n+1} and b_{n+1} are decoupled and may be solved independently.

As in the inhibitory map, the same issues arise given the implicit nature of the map. Multivalued solutions are a concern due to the mix of space scales in the excitatory and inhibitory terms in both equations. If the relative strength and extent of the excitatory synaptic coupling in one population is significantly larger than that of the inhibitory synaptic coupling, then, under the assumptions on w_{uv} and I_u, it is possible to create a cubic-shaped segment of the graph of either function F_e or F_i which has the potential of creating three zeros depending on the values of θ_u. If F_u crosses 0 at three points $x_1 < x_2 < x_3$, it means that regions $[0, x_1)$ and (x_2, x_3) are superthreshold and firing action potentials, whereas the interval (x_1, x_2) is subthreshold. It is also possible to get three zeros in the inhibitory map with σ_i sufficiently large, but the excitatory synaptic currents in the E-I map contribute to this effect dynamically depending on the activity in the excitatory population. Such behavior is, in fact, seen in conductance-based models when the extent of excitation exceeds that of inhibition and the excitatory connections are sufficiently strong to generate action potentials. However, such solutions violate the basic assumption of the construction of the map which requires at most a single band of cells to fire action potentials.

Linear stability of a fixed point. Let $(\bar{a}, \bar{b})$ be a fixed point of the E-I map, and let (φ_n, ψ_n) be a small perturbation so that

$$a_n = \bar{a} + \varphi_n, \qquad b_n = \bar{b} + \psi_n.$$

Expanding F_e, F_i in Taylor series about $(\bar{a}, \bar{b})$, the perturbations to first order satisfy

$$\begin{aligned} D_1 F_e^* \varphi_n + D_2 F_e^* \psi_n + D_3 F_e^* \varphi_{n+1} &= 0, \\ D_1 F_i^* \varphi_n + D_2 F_i^* \psi_n + D_3 F_i^* \psi_{n+1} &= 0, \end{aligned}$$

with

$$D_k F_e^* = D_k F_e(\bar{a}, \bar{a}, \bar{b}), \quad D_k F_i^* = D_k F_i(\bar{a}, \bar{b}, \bar{b}), \qquad k = 1, 2, 3.$$

The linearized map for the evolution of the perturbations is thus given by

$$\begin{pmatrix} \varphi_{n+1} \\ \psi_{n+1} \end{pmatrix} = M \begin{pmatrix} \varphi_n \\ \psi_n \end{pmatrix}, \qquad M = \begin{bmatrix} -\frac{D_1 F_e^*}{D_3 F_e^*} & -\frac{D_2 F_e^*}{D_3 F_e^*} \\ -\frac{D_1 F_i^*}{D_3 F_i^*} & -\frac{D_2 F_i^*}{D_3 F_i^*} \end{bmatrix},$$

provided that $D_3F^*_{e,i} \neq 0$, with the elements of M given by

$$\begin{aligned} D_1F_e^* &= D_2J_{ee}(\bar{a},\bar{a}), & D_1F_i^* &= D_2J_{ie}(\bar{b},\bar{a}),\\ D_2F_e^* &= -D_2J_{ei}(\bar{a},\bar{b}), & D_3F_e^* &= D_1J_{ee}(\bar{a},\bar{a}) - D_1J_{ei}(\bar{a},\bar{b}) + I_e'(\bar{a}),\\ D_2F_i^* &= -D_2J_{ii}(\bar{b},\bar{b}), & D_3F_i^* &= D_1J_{ie}(\bar{b},\bar{a}) - D_1J_{ii}(\bar{b},\bar{b}) + I_i'(\bar{b}). \end{aligned}$$

For general weight functions w_{uv}, where $u, v \in \{e, i\}$, we easily calculate

$$\begin{aligned} D_1J_{uv}(x,y) &= -g_{uv}\big(w_{uv}(x-y) - w_{uv}(x+y)\big),\\ D_2J_{uv}(x,y) &= +g_{uv}\big(w_{uv}(x-y) + w_{uv}(x+y)\big). \end{aligned}$$

Since the map is planar, we can express the two eigenvalues more practically as

$$\lambda_\pm = \frac{1}{2}\Big(\mathbf{tr}\, M \pm \sqrt{(\mathbf{tr}\, M)^2 - 4\,\mathbf{det}\, M}\Big).$$

4.2. Numerical solutions of the E-I map. All numerical simulations performed on the E-I map were in the case of Gaussian synaptic weights and inputs

$$w_{uv}(x) = \frac{1}{\sqrt{\pi}\sigma_{uv}}\exp\left(-\frac{x^2}{\sigma_{uv}^2}\right), \qquad \hat{I}_u(x) = I_u\exp\left(-\frac{x^2}{\sigma_u^2}\right),$$
$$J_{uv}(x,y) = \frac{g_{uv}}{2}\left[\operatorname{erf}\left(\frac{x+y}{\sigma_{uv}}\right) - \operatorname{erf}\left(\frac{x-y}{\sigma_{uv}}\right)\right], \qquad u, v \in \{e, i\}.$$

Only excitatory inputs $I_e, I_i > 0$ were considered, and θ_e, θ_i were taken to be in the range $(0, 1)$ given the FI-curve (Figure 6(a)) for the conductance-based model. The vast number of parameters makes it difficult to describe comprehensively when solutions exist; however, when solutions did exist, it was found that the E-I map commonly produced single-valued solutions across large parameter regions (though some exceptions were found). This was determined by inspecting graphs of the functions $F_e(a_n, b_n, x), F_i(a_n, b_n, x)$ for zero-crossings on each iterate.

As expected, fixed points and period 2 orbits, generated through flip bifurcations, were common as attracting sets of the E-I map. However, we investigated what other types of bifurcations were present in the two-dimensional map. Linear stability analysis predicted that Neimark–Sacker bifurcations would occur in various regions of parameter space; however, numerical solutions around many of these bifurcation points suggested the bifurcations were subcritical, leading to oscillations that grew exponentially until the map broke down as one of the variables approached 0. In two cases that were deemed supercritical by exhibiting a very small-amplitude invariant circle beyond the predicted bifurcation point, varying the bifurcation parameter further caused the invariant circle to grow rapidly with one of the half-widths a_n or b_n approaching 0. However, one particularly interesting region, with solutions bounded away from 0, unfolded various Neimark–Sacker bifurcations with both weak and strong resonance bifurcations, as illustrated in Figure 8 below. This revealed a dynamically rich parameter region in which to look for stable oscillatory solutions in the conductance-based model (see section 4.3). Various stable periodic orbits of higher order were also found in this region of the E-I map that bifurcated into what appeared to be strange attractors. In section 4.4, we describe perhaps the most interesting bifurcation observed in the E-I map, occurring in a different parameter region in which $\sigma_{ee} < \sigma_{ei}$ and $\sigma_{ie} > \sigma_{ii}$.

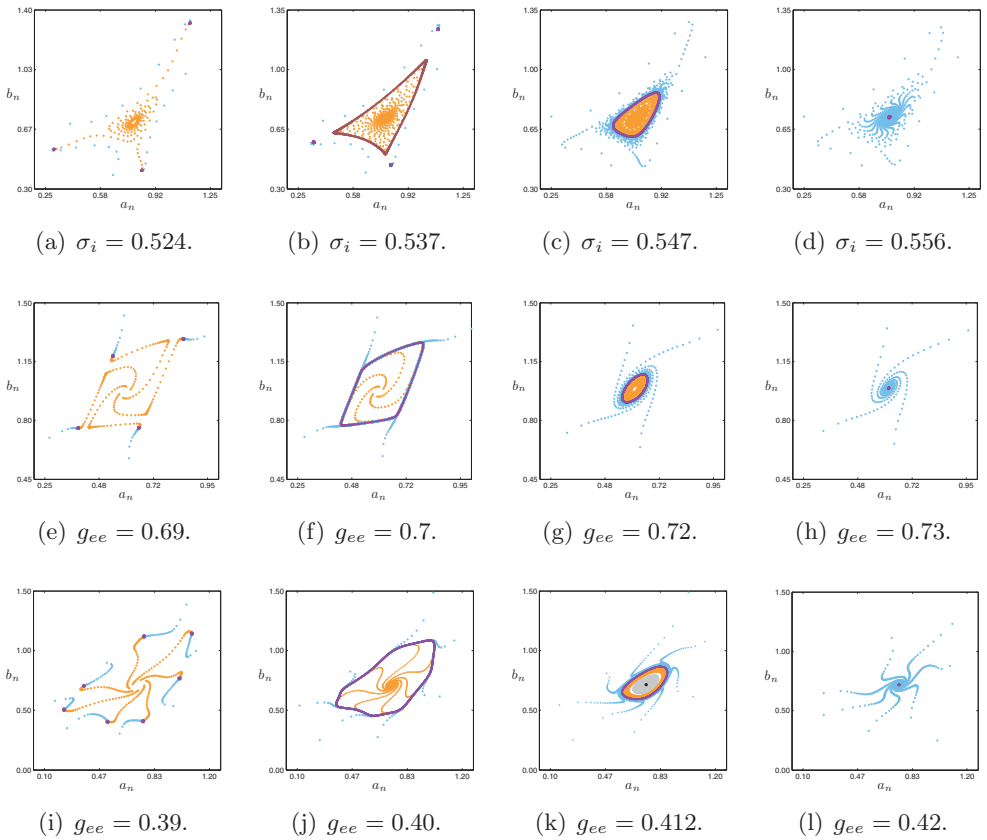

(a) $\sigma_i = 0.524$. (b) $\sigma_i = 0.537$. (c) $\sigma_i = 0.547$. (d) $\sigma_i = 0.556$.

(e) $g_{ee} = 0.69$. (f) $g_{ee} = 0.7$. (g) $g_{ee} = 0.72$. (h) $g_{ee} = 0.73$.

(i) $g_{ee} = 0.39$. (j) $g_{ee} = 0.40$. (k) $g_{ee} = 0.412$. (l) $g_{ee} = 0.42$.

Figure 8. *Neimark–Sacker bifurcation of fixed points in the E-I map, giving rise to various resonances of order q. Values for the bifurcation parameter are listed in the captions of each figure. Each figure depicts two orbits in the (a_n, b_n) phase plane, and each orbit is colored partially with a lighter color to indicate transients and partially with a darker color to indicate the set to which the orbit is attracted. One trajectory, colored with an orange transient and dark red ω-limit set, starts from an initial condition near the equilibrium in the center. The other trajectory, colored with light blue transient and dark purple ω-limit set, starts from the periphery. When the dark purple and dark red ω-limit sets coincide, only the dark purple is shown. The exception is panel* (k)*, in which the orange and light blue orbits approach the purple invariant circle while an additional gray transient approaches the stable equilibrium (black dot) at the center. The white ring indicates the presence of an unstable invariant circle. The emergence of a stable-unstable pair of invariant circles is characteristic of a generalized Neimark–Sacker bifurcation. Panels* (a)–(d) *illustrate a* 1:3 *resonance occurring for the parameter set $g_{ee} = 0.27$, $g_{ei} = 1$, $g_{ie} = 1.5$, $g_{ii} = 1.5$, $\theta_e = \theta_i = 0.23$. Panels* (e)–(h) *illustrate a* 1:4 *resonance bifurcation occurring for the set $g_{ei} = 1.07$, $g_{ie} = 3$, $g_{ii} = 1.2$, $\theta_e = \theta_i = 0.28$, $\sigma_i = 0.5$. Panels* (i)–(l) *illustrate a* 1:7 *resonance occurring for the set $g_{ei} = 1.1$, $g_{ie} = 1.485$, $g_{ii} = 1.25$, $\theta_e = \theta_i = 0.265$, $\sigma_i = 0.5$. Parameters common to all figures are given by $\sigma_{ee} = \sigma_{ie} = \sigma_{ei} = \sigma_{ii} = 1$ and $I_e = 1$, $I_i = 1$, $\sigma_e = 1$.*

Note on resonances. Resonances occur as a special case of the Neimark–Sacker bifurcation in which the linearized map about a simple fixed point has a pair of eigenvalues that are qth roots of unity [26]. Occurring for $q \geq 5$, a *weak resonance* is an interdigitated pair of period q orbits (one of q saddles, one of q nodes), which together can form a closed invariant curve from heteroclinic connections between adjacent saddle and node periodic points; the stable and unstable manifolds of the saddles separate the q suborbits as each approaches its

respective stable node. In two-parameter unfoldings of the bifurcation, each root of unity gives rise to a weak resonance and its associated Arnold tongue, a cusp-like region which emerges outward from the unit circle, the interior of which is the existence region for the resonance. The boundary of the tongue corresponds to a saddle-node bifurcation through which the periodic orbits emerge and vanish. For parameters near the boundary but exterior to the Arnold tongue, it is possible for iterates of the map to spend time in the vicinity of the emerging saddle-node before approaching another solution. *Strong resonances* occur when $q = 1, 2, 3, 4$, in which a more complicated codimension 2 bifurcation structure may arise from additional degeneracies associated with these eigenvalues.

4.3. Comparison with the conductance-based model. A variety of qualitative comparisons may be made between the localized synchronous oscillations in the E-I map and in the associated conductance-based model. We summarize a few here. In the conductance-based model, we considered excitatory synapses with a decay time constant consistent with the AMPA receptor type ($\beta_e = 0.5$–1.0). Sufficiently strong inhibition to both populations was used to ensure that the spatiotemporal solutions were clean and regular for comparison with the map. When the conductance-based model supported a localized band of oscillations, with the ambient medium quiescent, the width of the band typically approached either fixed width solutions or an alternation between two widths with a exponential decay to the steady solution that was qualitatively similar to the E-I map. Therefore fixed points and period 2 orbits were common localized solutions in both models.

The E-I map, additionally, can reflect the effect of runaway excitation; this occurs in the conductance-based model, for example, when increasing the coupling strength g_{ee}^c of the e-to-e connections induces an instability of the localized region of synchronized oscillations, resulting in an a ever-widening region of persistent spiking activity. Correspondingly, in the E-I map, it was possible to show in some cases that, by increasing g_{ee}, a stable fixed point underwent a fold bifurcation corresponding to a $\lambda = 1$ eigenvalue. Also, when a period 2 orbit was present in numerical simulations of the E-I map, increasing g_{ee} in many cases led to an apparent instability of the periodic orbit in which the solution continued to alternate with two suborbits with the value of a_n monotonically increasing.

The time constant of decay β_e^{-1} associated with the excitatory AMPA synapses is short relative to the period of the gamma cycle, so that, by the end of the gamma cycle, it has decayed considerably more than inhibition. Therefore, either the excitatory synaptic strengths in the E-I map should be taken to be small (since we assumed that they are defined by the synaptic currents at the end of the cycle in the derivation of the map) or, instead, they are interpreted more abstractly in an *effective* sense. We note that such excitatory currents in the conductance-based model also can contribute to spiking during the early phase of the gamma cycle in a way similar to the early-cycle inhibition discussed in Figure 6. Our investigation was limited only to synchronous spiking patterns that strongly conformed to the assumptions of the map, and, for β_e^{-1} in the range of AMPA-mediated synaptic currents, the boundaries of the spiking region did not display any well-defined oscillatory behavior.

Subsequently, β_e^{-1} was increased in the conductance-based model to be on the order of the decay time constant of inhibition in order to reduce the disparity between the inhibitory and excitatory synaptic currents at the end of the cycle. Accordingly, the synaptic strength g_{ee}^c was kept sufficiently small to prevent reexcitation prior to the end of the gamma cycle. In

a parameter region related to that described in section 4.4 for the E-I map, we set $\beta_e = 0.19$ in the conductance-based model and found that that a steady fixed width solution underwent two flip bifurcations, first to a period 2 orbit and, subsequently, to a well-defined and regular period 4 orbit. However, varying parameters further led to instability of the steady solution such that the boundaries of the excited region expanded in an exponential fashion, leaving a highly complex spiking pattern in the interior. Increased spatial resolution is necessary to resolve orbits with increasingly complex structure, which is compounded by the fact that the conductance-based model must evolve over a considerable interval of time to generate the equivalent of each iteration of the map.

Neimark–Sacker and 1:5 resonance in the conductance-based model. The decay time constant of the excitatory synapses was increased further to 8 ms ($\beta_e = 0.123$) (note that GABA_A inhibition has a decay time constant of 10 ms), and examination of the parameter region suggested by the results in Figure 8 revealed a region exhibiting rich dynamics. Figure 9 illustrates a set of simulations of the conductance-based model which are suggestive of a Neimark–Sacker bifurcation giving rise to an invariant circle with 1:5 resonances. Near this point in the conductance-based model lies a region of complicated dynamics, parallel to the related region in the E-I map. However, higher resolution simulations are necessary to adequately resolve the dynamics in this region.

4.4. A strong (1:2) resonance bifurcation of a period 2 orbit. In this section, we describe an interesting example of nontrivial dynamics exhibited by the E-I map (4.2) in the vicinity of what numerical simulations and linear stability analysis indicate is codimension 2 strong resonance bifurcation. Although typically described as a bifurcation of a fixed point, in this case the 1:2 resonance bifurcation occurs on a period 2 orbit wherein each periodic point independently undergoes a 1:2 resonance bifurcation. In the numerical simulations of the E-I map, we describe the codimension 2 bifurcation in terms of the pair of parameters (σ_{ii}, θ_i), though many pairs of parameters unfold this bifurcation. For some ranges of these parameters, the attracting sets of the 1:2 resonance are surrounded by a large strange attractor formed of Hénon-like curves, which we call the *seahorse attractor*. Once the attracting sets of the 1:2 resonance vanish, the unstable region approaches the seahorse attractor.

A 1:2 resonance bifurcation occurs when the discrete map linearized about a fixed point contains the eigenvalue pair $\lambda_{1,2} = -1$ and is included among the strong resonance bifurcations ($q = 2$) which have a more complicated codimension 2 bifurcation structure involving homoclinic and/or heteroclinic connections. Strong resonances occur in Poincaré maps associated with systems exhibiting two independent frequencies and commonly have been found in periodically driven nonlinear oscillators, e.g., the Van der Pol equation or Duffing's equation [14]. Although the inputs in our system are not periodic in time, the time-independent input drives the inhibitory population which organizes the synchronous oscillation in both populations through strong synaptic inhibition.

The classical approach to studying many of the codimension 2 bifurcations of two-dimensional discrete maps considers the time-T map that samples periodically, with period T, an approximating vector field known as an equivariant versal unfolding [1, 4, 17]. Normal forms, including explicit formulas for the critical coefficients of the resonant terms, have been derived for most of the codimension 2 bifurcations, including the strong resonances; see [19, 18, 17]. These normal forms capture all local bifurcations but, in some cases, are incom-

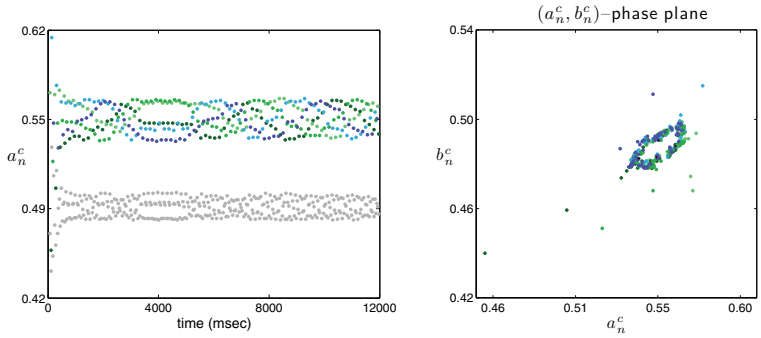

(a) $g_{ee}^c = 0.5$.

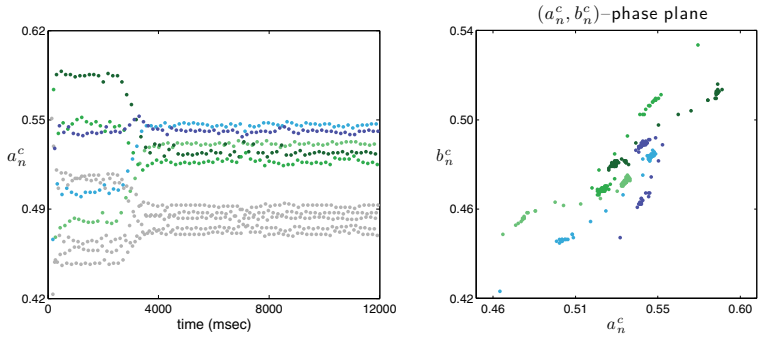

(b) $g_{ee}^c = 0.48$.

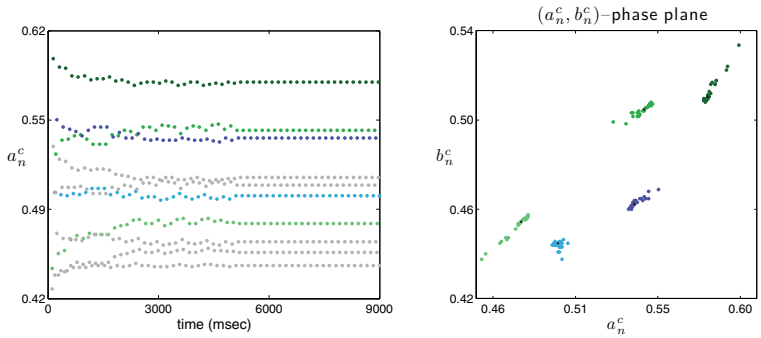

(c) $g_{ee}^c = 0.47$.

Figure 9. *Neimark–Sacker bifurcation and* 1:5 *resonance in the conductance-based model in a parameter region related to those in Figure* 8 *in the E-I map. Every fifth iterate is colored identically to illustrate that the synchronous oscillations in the conductance-based model behave like the five suborbits in a discrete map during a* 1:5 *weak resonance. Left column: solution plots of the halfwidth* a_n^c *(color) in the excitatory population and* b_n^c *(gray) in the inhibitory population. Right column: corresponding orbits in the* (a_n^c, b_n^c) *phase plane.* (a) *Beyond the (assumed) Neimark–Sacker bifurcation point, a transient initially spends time near the ghost of a small period* 5 *orbit and, subsequently, approaches an invariant circle.* (b) *A transient approaches and spends time near the ghost of a large* 1:5 *resonance, and, subsequently, approaches the smaller* 1:5 *resonance inside.* (c) *The system now approaches the large* 1:5 *resonance where the slowdown occurred in* (b). *Other parameters are* $I_e^c = 1$, $I_i^c = 1$, $\sigma_e^c = 1$, $\sigma_i^c = 0.5$, $g_{ei}^c = 2$, $g_{ie}^c = 1.5$, $g_{ii}^c = 3$, $\sigma_{ee}^c = \sigma_{ei}^c = \sigma_{ie}^c = \sigma_{ii}^c = 1$, $\beta_e = 0.123$, *with other parameters listed in Appendix* A. *The oscillation frequency is approximately* 28–30 *Hz.*

plete due to the fact that higher order terms govern global phenomena, such as homoclinic and heteroclinic intersections, which can occur. In some cases, for example, the generalized Hénon map can be used to understand the dynamics near homoclinic and heteroclinic tangencies occurring in various two-parameter discrete maps [12]. Though it is perhaps more appropriate to study the normal form map, the bifurcation diagram of the approximating vector field, shown in Figure 10, provides an accessible geometric view into the set of bifurcations present in a 1:2 resonance bifuraction, thereby facilitating the description of the numerical simulations of the E-I map.

Initial numerical evidence suggesting a 1:2 resonance. Two consecutive flip bifurcations of a fixed point leading to a period 4 orbit were explored in numerical simulations of the E-I map in order to pursue further bifurcations thereof. Since there are many parameters, the parameters were fixed at the values given in Figure 13(a), and the same two consecutive flip bifurcations of a fixed point to a period 4 orbit were reproduced by increasing only the spatial extent σ_{ie} of the e-to-i connections through the interval $\sigma_{ie} \in [1, 2.91]$. Increasing σ_{ie} to 2.915 subsequently led to a Neimark–Sacker bifurcation of the period 4 orbit, producing four invariant circles, as shown in Figure 13(a). Fixing $\sigma_{ie} = 2.915$ and decreasing θ_i from 0.25 to 0.191 led through a sequence of higher order resonances intermixed with short intervals with an apparent strange attractor having four *batwing* shapes, each resembling the undulating shape of the unstable manifolds of the period 2 orbit (saddles) near a homoclinic tangency (see Figure 13(b)). This sequence shares some characteristics with the sequence described in the delayed logistic map [2] and the Bogdanov map [3]. Notice that the batwing attractor is very close to $b_n = 0$, causing solutions in the map to break down when θ_i is decreased much further.

To move the attracting sets away from $b_n = 0$, the strength of i-to-i inhibition was set to $g_{ii} = 1.5$, and its spatial extent was increased to $\sigma_{ii} = 1.6$. This brought the system to a parameter region, whereupon decreasing θ_i towards $\theta_i \approx 0.17392$ led to the merging of the four invariant circles into two large invariant circles, one of which is shown in Figure 13(c). Figure 13(d) illustrates an analogous merging for fixed $\sigma_{ii} = 1.575$, in which case decreasing θ_i led to a complex trajectory resembling unstable manifolds in the schematic of the double homoclinic tangle in Figure 12. This suggests that the system is near the codimension 2 point in the (σ_{ii}, θ_i) plane of a 1:2 resonance bifurcation occurring on a period 2 orbit, which we now substantiate using linear stability analysis.

Linear stability analysis of period 2 orbits in the E-I map. We derive conditions for the existence and linear stability of a period 2 orbit to verify the eigenvalue structure ($\lambda_{1,2} = -1$) of the 1:2 resonance in the vicinity of the parameter region described in Figure 13. Let $(\bar{a}_1, \bar{b}_1)$ and $(\bar{a}_2, \bar{b}_2)$ define the period 2 orbit, i.e.,

$$(a_{2n}, b_{2n}) = (\bar{a}_1, \bar{b}_1), \quad (a_{2n+1}, b_{2n+1}) = (\bar{a}_2, \bar{b}_2) \qquad \text{for all } n \in \mathbb{Z}^+.$$

Since each periodic point of the period 2 orbit is a fixed point of the E-I map composed with itself, the period 2 orbit satisfies the following equations simultaneously:

$$\begin{aligned} F_e(\bar{a}_1, \bar{b}_1, \bar{a}_2) &= 0, \qquad F_e(\bar{a}_2, \bar{b}_2, \bar{a}_1) = 0, \\ F_i(\bar{a}_1, \bar{b}_1, \bar{b}_2) &= 0, \qquad F_i(\bar{a}_2, \bar{b}_2, \bar{b}_1) = 0. \end{aligned} \tag{4.3}$$

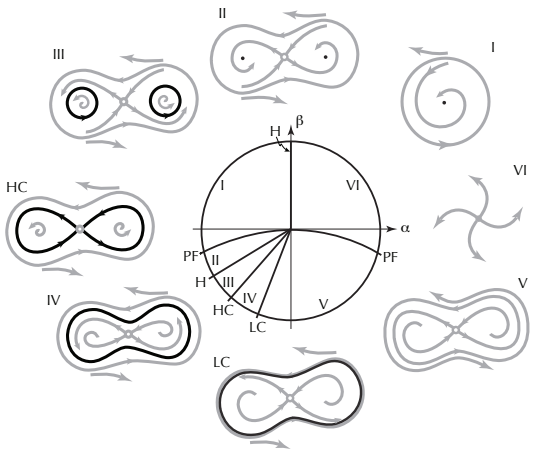

Figure 10. *A useful geometric picture of the bifurcations in the* 1:2 *resonance bifurcation in a discrete map is provided by the bifurcation diagram of an approximating vector field* $x' = \alpha x + (1+\beta)y + x^3$, $y' = -\beta x + \alpha y + \delta x^3$ $(\delta = -1)$, *which unfolds a Bogdanov–Takens bifurcation in a system with* $\mathbb{Z}_2$ *symmetry* [4, 24, 17]. *Black curves indicate attracting sets, chosen to reflect the numerical results of the E-I map. Summary of the bifurcations in a counterclockwise loop around the codimension* 2 *point at the origin, beginning with region* I, *which corresponds to the starting point of our description of the simulations of the E-I map: In region* I *a stable equilibrium is surrounded by an unstable limit cycle. Passing from region* I *to* II *across curve PF, the stable fixed point undergoes a supercritical pitchfork bifurcation (reflecting the* $\mathbb{Z}_2$ *symmetry), yielding two stable fixed points separated by a saddle point. Both stable equilibria undergo supercritical Hopf bifurcations as one traverses from region* II *to* III *across curve H, giving rise to a pair of stable limit cycles, with the large unstable limit cycle still present. As one moves towards curve HC, the limit cycles grow in size, ultimately resulting in a pair of stable homoclinic connections of the saddle. Traversing the curve HC of homoclinic points, the pair of limit cycles join together to form one large limit cycle. Approaching curve LC in region* IV, *this large stable limit cycle continues to grow towards the surrounding unstable limit cycle until it coalesces into a single cycle which is stable only from within, as indicated by the half black, half gray curve in diagram LC. The cycle vanishes in a saddle-node bifurcation of limit cycles, leaving a saddle and two unstable equilibria. Crossing curve PF from region* V *into region* VI, *the unstable equilibria collide with the saddle in a subcritical pitchfork bifurcation, yielding a single unstable equilibrium. Finally, traversing curve H from region* VI *to* I, *the unstable equilibrium undergoes a subcritical Hopf bifurcation.*

Interpretation for the discrete map: The pitchfork and Hopf bifurcations correspond to flip and Neimark–Sacker bifurcations, respectively, in the map. The homoclinic connections that form in the map need not *coincide everywhere and are governed generically by higher order terms. Instead, the stable and unstable manifolds initially form tangencies at infinitely many isolated points which accumulate in both directions at the saddle point—these correspond to the forward and backward iterates of the map. The manifolds proceed to pass through each other, forming infinitely many transverse intersections until a final tangency is reached. For such transverse intersections to occur, the manifolds must fold, shrink, and stretch wildly, producing a structure known as a* homoclinic tangle, *which is* partially *sketched in Figure 11. Such structures have been shown to contain Smale horseshoe maps that give rise to intricate dynamics and chaos. In the* 1:2 *resonance bifurcation, a* double homoclinic tangle *arises, due to the* $\mathbb{Z}_2$ *symmetry in the system, and is partially drawn in Figure 12. In contrast to differential equations, the homoclinic connections that form in discrete maps, generically, are structurally stable, and consequently the curve HC of homoclinic connections for the approximating system becomes a tongue, or* wedge, *of homoclinic intersections that issues from the codimension* 2 *point in the discrete map. The boundaries of the wedge correspond to the initial and final tangencies. Curve LC similarly implies a wedge since, generically, the coalescing stable and unstable invariant curves in region* IV *also ultimately intersect transversally as they pass through one another. These intersections can lead to weak resonances, and homoclinic and heteroclinic tangles may form between the periodic points* [4].

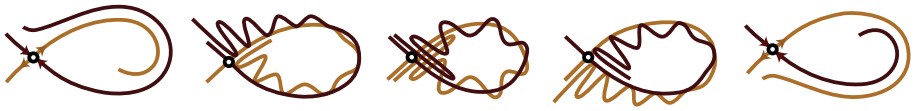

Figure 11. *Homoclinic bifurcation for a discrete map* [26]. *Generically, the stable manifolds (darker color) and the unstable manifolds (lighter color) form infinitely many transverse intersections (homoclinic points) that accumulate at the saddle point, resulting in a homoclinic tangle that is structurally stable and persists over a range of parameter values. The initial and final points of tangency define the boundaries of the parameter region which can take the shape of a horn or wedge issuing from a codimension* 2 *bifurcation point. Such structures were first described by Poincaré in* 1890.

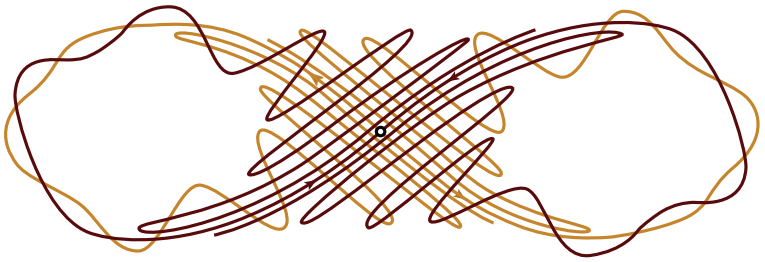

Figure 12. *Double homoclinic tangle (caricature) arising in a* 1:2 *resonance bifurcation. The stable manifolds (darker color) and the unstable manifolds (lighter color) are only partially drawn and continue to fold and wrap around both the interior and exterior of the structure. The attracting set in the E-I map bears a strong resemblance to the geometry of the unstable manifold.*

Consider the evolution of small perturbations $(\varphi_n, \psi_n)^{\mathrm{T}}$ of the period 2 orbit. Define

$$\begin{aligned}(a_{2n}, b_{2n}) &= (\bar{a}_1 + \varphi_{2n}, \bar{b}_1 + \psi_{2n}),\\ (a_{2n+1}, b_{2n+1}) &= (\bar{a}_2 + \varphi_{2n+1}, \bar{b}_2 + \psi_{2n+1}) \qquad \text{for all } n \in \mathbb{Z}^+.\end{aligned}$$

The perturbations about the period 2 orbit satisfy the following for all $n \in \mathbb{Z}^+$:

$$\begin{aligned}F_e\big(\bar{a}_1 + \varphi_{2n},\, \bar{b}_1 + \psi_{2n},\, \bar{a}_2 + \varphi_{2n+1}\big) &= 0,\\ F_i\big(\bar{a}_1 + \varphi_{2n},\, \bar{b}_1 + \psi_{2n},\, \bar{b}_2 + \psi_{2n+1}\big) &= 0,\\ F_e\big(\bar{a}_2 + \varphi_{2n+1},\, \bar{b}_2 + \psi_{2n+1},\, \bar{a}_1 + \varphi_{2n+2}\big) &= 0,\\ F_i\big(\bar{a}_2 + \varphi_{2n+1},\, \bar{b}_2 + \psi_{2n+1},\, \bar{b}_1 + \psi_{2n+2}\big) &= 0.\end{aligned}$$

Expanding the nonlinearities in a Taylor series, through first order in (φ_n, ψ_n), and applying the conditions (4.3) for the period 2 orbit results in

$$\begin{aligned}D_1F_e^{*1}\,\varphi_{2n} &+ D_2F_e^{*1}\,\psi_{2n} &+ D_3F_e^{*1}\,\varphi_{2n+1} &= 0,\\ D_1F_i^{*1}\,\varphi_{2n} &+ D_2F_i^{*1}\,\psi_{2n} &+ D_3F_i^{*1}\,\psi_{2n+1} &= 0,\\ D_1F_e^{*2}\,\varphi_{2n+1} &+ D_2F_e^{*2}\,\psi_{2n+1} &+ D_3F_e^{*2}\,\varphi_{2n+2} &= 0,\\ D_1F_i^{*2}\,\varphi_{2n+1} &+ D_2F_i^{*2}\,\psi_{2n+1} &+ D_3F_i^{*2}\,\psi_{2n+2} &= 0.\end{aligned}$$

where, for $k = 1, 2, 3$,

$$D_kF_{e,i}^{*1} = D_kF_{e,i}(\bar{a}_1, \bar{b}_1, \bar{a}_2), \qquad D_kF_{e,i}^{*2} = D_kF_{e,i}(\bar{a}_2, \bar{b}_2, \bar{a}_1).$$

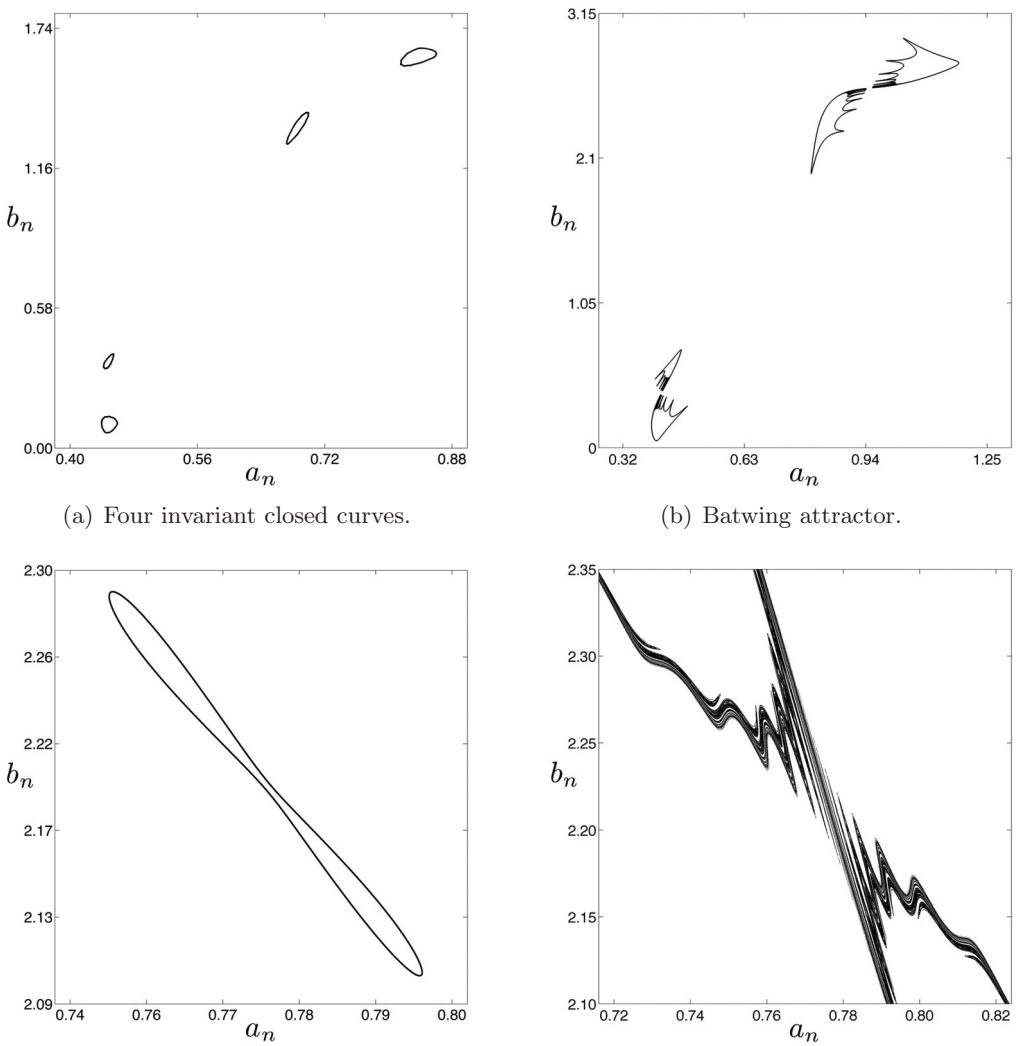

(a) Four invariant closed curves.

(b) Batwing attractor.

(c) Stable closed curve.

(d) Double homoclinic tangle.

Figure 13. *Attracting sets in numerical simulations of the E-I map suggestive of a* 1:2 *resonance bifurcation occurring on a period* 2 *orbit. Each panel depicts a single orbit in the* (a_n, b_n) *phase plane after removal of the transient originating near the unstable period* 4 *orbit that lies inside the attracting sets depicted.* (a) *A stable attracting solution composed of four invariant closed curves beyond a supercritical Neimark–Sacker bifurcation occurring on a period* 4 *orbit. Parameters:* $g_{ii} = 1.8$, $\sigma_{ii} = 1.5$, $\theta_i = 0.25$. (b) *Decreasing* θ_i *from its value in* (a), *keeping other parameters fixed, results in an intricate attracting set composed of four batwing-shaped curves, with every fourth iterate visiting one of them. Up close, the batwing attractor reveals that each curve is composed of many tightly packed curves typical of strange attractors. Parameters:* $g_{ii} = 1.8$, $\sigma_{ii} = 1.5$, $\theta_i = 0.191$. (c) *One of two (other hidden) large invariant closed curves each resulting from the coalescence of two smaller closed invariant curves for* $g_{ii} = 1.5$, $\sigma_{ii} = 1.6$, $\theta_i = 0.17392$. (d) *Decreasing* σ_{ii} *from that in* (c) *reveals a highly complex single orbit reflecting the geometry of the unstable manifolds of one of two (other hidden) double homoclinic tangles for* $g_{ii} = 1.5$, $\sigma_{ii} = 1.575$, $\theta_i = 0.18115$. *Common (fixed) parameters for all figures:* $g_{ee} = 1.0$, $g_{ei} = 1.8$, $g_{ie} = 3$, $\sigma_{ee} = 0.8$, $\sigma_{ei} = 2.1$, $\sigma_{ie} = 2.915$, $I_e = 1.1$, $I_i = 1.0$, $\sigma_e = 0.9$, $\sigma_i = 1.2$, $\theta_e = 0.25$.

The linearized map for the evolution of the perturbations (φ_n, ψ_n) is then given by

$$\begin{pmatrix} \varphi_{2n+1} \\ \psi_{2n+1} \end{pmatrix} = M_1 \begin{pmatrix} \varphi_{2n} \\ \psi_{2n} \end{pmatrix}, \qquad M_1 = \begin{bmatrix} -\frac{D_1 F_e^{*1}}{D_3 F_e^{*1}} & -\frac{D_2 F_e^{*1}}{D_3 F_e^{*1}} \\ -\frac{D_1 F_i^{*1}}{D_3 F_i^{*1}} & -\frac{D_2 F_i^{*1}}{D_3 F_i^{*1}} \end{bmatrix} \tag{4.4}$$

and

$$\begin{pmatrix} \varphi_{2n+2} \\ \psi_{2n+2} \end{pmatrix} = M_2 \begin{pmatrix} \varphi_{2n+1} \\ \psi_{2n+1} \end{pmatrix}, \qquad M_2 = \begin{bmatrix} -\frac{D_1 F_e^{*2}}{D_3 F_e^{*2}} & -\frac{D_2 F_e^{*2}}{D_3 F_e^{*2}} \\ -\frac{D_1 F_i^{*2}}{D_3 F_i^{*2}} & -\frac{D_2 F_i^{*2}}{D_3 F_i^{*2}} \end{bmatrix}, \tag{4.5}$$

where the elements of M_1 and M_2 are expressed in terms of the currents J_{uv} in Appendix B.

Composing the maps in (4.4) and (4.5), the linearized map for the perturbations associated with the even periodic points of the period 2 orbit is

$$\begin{pmatrix} \varphi_{2n+2} \\ \psi_{2n+2} \end{pmatrix} = M_\circ \begin{pmatrix} \varphi_{2n} \\ \psi_{2n} \end{pmatrix}, \qquad M_\circ = M_2 M_1.$$

Odd iterates satisfy the same map with $M_\circ$ interchanged with $M_\circ' = M_1 M_2$, and the eigenvalues of $M_1 M_2$ are the same as those of $M_2 M_1$.

With respect to the composition map, each of the periodic points is a fixed point, the linear stability of which is determined by the eigenvalues of the linearization of the composition matrix $M_\circ$. In particular, we expect a pair of eigenvalues $\lambda_{1,2} = -1$ in the vicinity of the region of parameter space investigated in Figures 13(d) and 13(c), corresponding to a 1:2 resonance bifurcation occurring on each of the periodic points. The conditions for a double eigenvalue $\lambda_{1,2} = -1$ of $M_\circ$ can be expressed as

$$\mathbf{tr}(M_\circ) = -2, \qquad \mathbf{det}(M_\circ) = 1. \tag{4.6}$$

Since we do not have analytical expressions for the period 2 orbit, we determine it by solving (4.3) numerically and, subsequently, calculate its eigenvalues. Therefore, finding a codimension 2 point where $M_\circ$ has a double eigenvalue $\lambda_{1,2} = -1$ requires solving the system of six nonlinear equations (4.3) and (4.6) for six unknowns. Four unknowns constitute the periodic orbit, and any two others serve as bifurcation parameters, with all other parameters set a priori. Using the parameter values listed in the captions of Figures 13(c) and 13(d) as the starting point for the numerical solution of (4.3)–(4.6), the codimension 2 point was calculated as $(\sigma_{ii}, \theta_i) \approx (1.60477, 0.17215)$ in the (σ_{ii}, θ_i) plane with other parameters fixed at $g_{ee} = 1.0$, $g_{ei} = 1.8$, $g_{ie} = 3$, $g_{ii} = 1.5$, $\sigma_{ee} = 0.8$, $\sigma_{ei} = 2.1$, $\sigma_{ie} = 2.915$, $I_e = 1.1$, $I_i = 1.0$, $\sigma_e = 0.9$, $\sigma_i = 1.2$, $\theta_e = 0.25$. This codimension 2 point can be continued as an organizing center for nontrivial dynamics in this region of parameter space.

Numerical results near the codimension 2 point. In the vicinity of the codimension 2 point in the (σ_{ii}, θ_i) plane, the behavior of the E-I map strongly reflects the results from bifurcation theory on the 1:2 resonance. Taking the codimension 2 point $(\sigma_{ii}, \theta_i) \approx (1.60477, 0.17215)$ as the origin of a local coordinate system in the (σ_{ii}, θ_i) plane, we consider region $\mathcal{S} = [1.575, 1.60477] \times [0.172, 0.5]$ in quadrant 2.

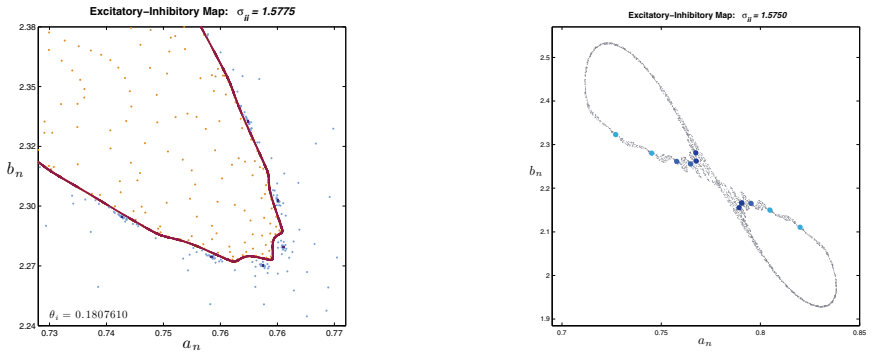

(a) Phase portrait animation. (b) Orbit near homoclinic tangle.

Figure 14. (a) *Snapshot from a movie of the E-I map composed of* 2850 *different phase portraits for* θ_i *decreasing from* 0.5 *to* 0.18 *and* $g_{ii} = 1.5$, $\sigma_{ii} = 1.5775$, *with other parameters listed in Figure* 13. *Orbits (up to* 100,000 *iterates) from two initial conditions are shown, with transients (orange/light blue) and long-term behavior (red/purple, with purple shown only if the two overlap). The bifurcation sequence contains* (1) *the initial flip bifurcation from the fixed point to the period* 2 *orbit, which subsequently undergoes the* 1:2 *resonance (as follows);* (2) *the supercritical flip bifurcation to the period* 4 *orbit;* (3) *the supercritical Neimark–Sacker bifurcation of the period* 4 *orbit, producing four invariant circles with subsequent weak resonance bifurcations;* (4) *the homoclinic bifurcation which generates the pair of double homoclinic tangles; and* (5) *the analogue of the saddle-node bifurcation of limit cycles. Beyond this, the region becomes unstable, and orbits approach the seahorse attractor.* (b) *Animation of the iterates of an orbit in the presence of the homoclinic tangles (only one shown), demonstrating how the set with* $\sigma_{ii} = 1.575$ *in Figure* 16 *is generated. Dark blue dots represent more advanced iterates. Click on the images above to see the accompanying movie files (*78009_01.avi [48.3MB] *and* 78009_02.avi [6.9MB]*).*

Figure 14(a) is an animated sequence of phase portraits for the case $\sigma_{ii} = 1.5775$ capturing the characteristic bifurcations (which are listed in the caption) in this region as θ_i is decreased from $\theta_i = 0.5$, where a stable fixed point exists, down below the point $\theta \approx 0.1805$, at which point the region has become unstable and trajectories flow out to the ambient region where the seahorse attractor lies. For sufficiently close initial conditions, orbits approaching the stable attracting sets of the 1:2 resonance were always single-valued and well-defined. However, for $\sigma_{ii} < 1.575$ the seahorse attractor progressively encroaches on the region.

Near the codimension 2 point, i.e., for $\sigma_{ii} \in [1.59, 1.6]$, the orbits resemble those of the approximating system, generally producing four invariant circles, a pair of double homoclinic loops (one shown in Figure 15(d)), and a pair of large invariant circles (one shown in Figure 13(c)). Decreasing σ_{ii} to move the system away from the codimension 2 point, the following were observed: (1) Weak resonances occur more commonly between the Neimark–Sacker and homoclinic bifurcations. Weak resonances bifurcate on the invariant circle, but they also may bifurcate adjacent to, and ultimately collide with, the invariant circle. In the latter case, prior to collision, the two cycles (one of spirals, the other of saddles) do not yet form a closed invariant curve, with the stable manifolds of the saddles separating orbits that approach either the invariant circles or the cycles of spirals. Higher order periodic orbits form and, at times, give way to complex sets which appear to be strange attractors. (2) Near the initial homoclinic tangency the attracting sets are heavily influenced by the undulations of the unstable manifold

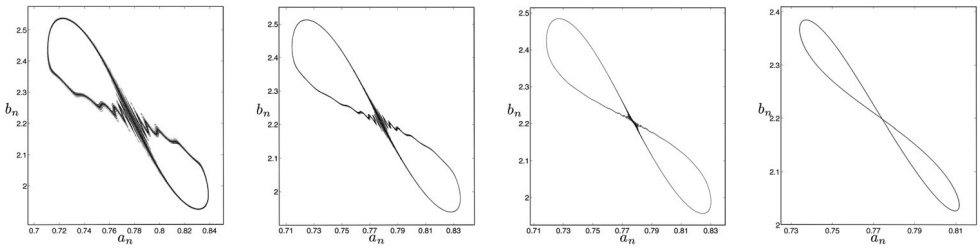

(a) $\sigma_{ii} = 1.575$. (b) $\sigma_{ii} = 1.5775$. (c) $\sigma_{ii} = 1.58$. (d) $\sigma_{ii} = 1.59$.

Figure 15. *A single orbit in the (a_n, b_n) phase plane of the E-I map for parameters in the interior of the wedge of existence of the homoclinic tangle which lies obliquely in the (σ_{ii}, θ_i) plane. As σ_{ii} is decreased from the codimension 2 point, θ_i must be tuned (increased) accordingly. Computed from the linearization about the period 2 orbit, the codimension 2 point occurs at $\sigma_{ii} \approx 1.60477$, $\theta_i \approx 0.17215$. Though not visible in plot* (d) *for $\sigma_{ii} = 1.59$, the wild oscillations are nonetheless present on a very small scale in the vicinity of the saddle. Other parameters listed in Figure 13.*

of the saddles (period 2 orbit); Figure 13(b) shows a more extreme version of this in the *batwing attractor*. Moving away from the codimension 2 point, orbits become increasingly intricate and folded near the homoclinic tangency and in the presence of the homoclinic tangle, as shown in Figure 15. Figure 16 depicts an intricate single orbit in the (a_n, b_n) phase plane seen at different levels of magnification for $\theta_i = 1.575$. (3) The analogue of the saddle-node bifurcation of limit cycles gives rise to weak resonances and increasingly intricate dynamics as well. A full circle of the bifurcation diagram can be performed by continuing along a curve about the codimension 2 point in the (σ_{ii}, θ_i) phase plane. Although there are no stable attracting sets associated with the 1:2 resonance until the Hopf bifurcation occurs, plotting trajectories for different initial conditions reveals behavior qualitatively similar to regions V and VI in Figure 10; i.e., it is possible to detect a saddle and two unstable spirals that undergo a symmetric flip bifurcation as well as the subcritical Neimark–Sacker bifurcation that defines the transition between regions VI and I.

Beyond the local structure of the 1:2 resonance. In the vicinity of the codimension 2 point, a large strange attractor appears which is separated from the attracting sets of the 1:2 resonance by the two unstable large invariant closed curves (see Figure 10). The *seahorse attractor*, formed from a multitude of Hénon-like curves, emerges from the vicinity of a large periodic orbit surrounding the two unstable closed curves (1:2 resonance). Approaching the seahorse attractor, the equation for b_{n+1} in (4.2) can have either one or three solutions. By choosing only one solution on each iteration, the orbit in the phase plane typically traces out a subset of the seahorse attractor with obvious parts of the attractor missing. The attracting set is quite intricate, and a complicated set of instructions was necessary to bias which of the three solutions were chosen to ensure that the missing parts of the attractor would be visited more often. Although multivalued solutions are irrelevant for a single band of synchronous oscillations, the seahorse attractor is nonetheless compelling in its own right. Figure 17 depicts a sequence of four stages of the seahorse attractor for the case $\sigma_{ii} = 1.5775$ and for $\theta_i < 0.18$, where the movie ends (see Figure 14(a)). The two oval-shaped regions contain the unstable period 2 and period 4 orbits, and the unstable fixed point lies in the center of the stem connecting them.

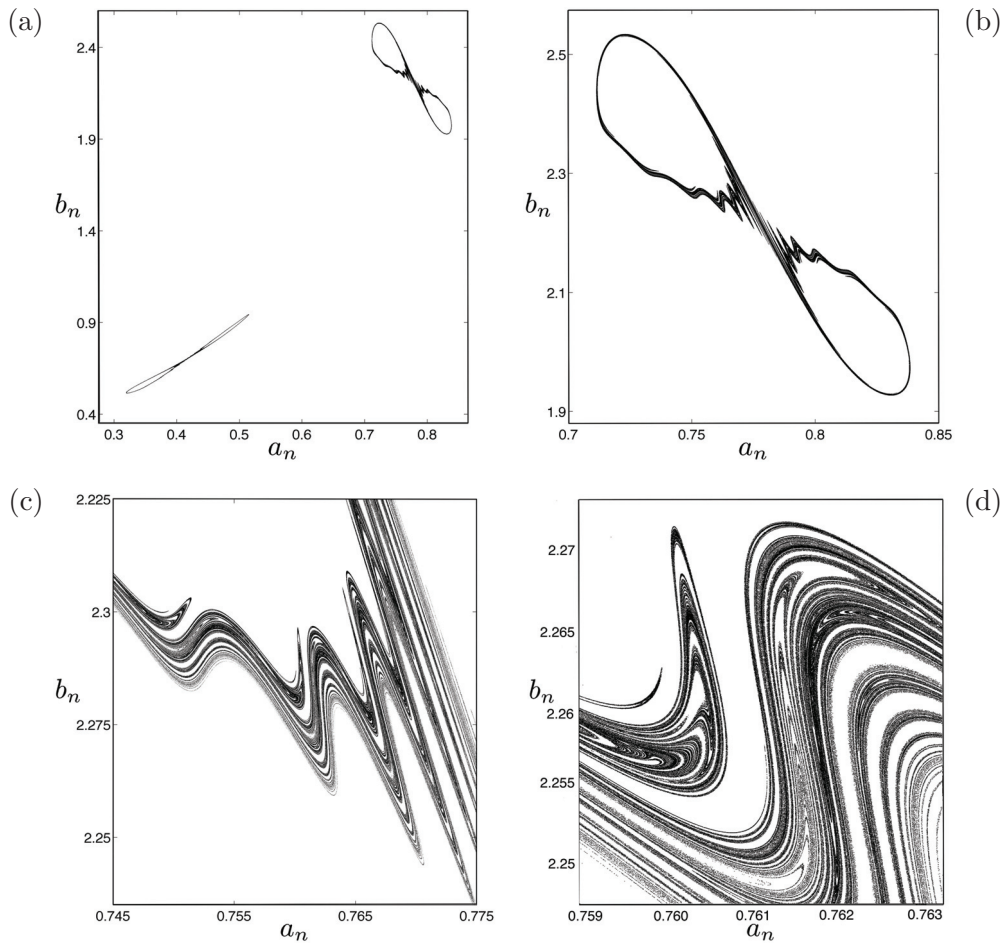

Figure 16. *A single orbit for* $g_{ii} = 1.5$, $\sigma_{ii} = 1.575$, $\theta_i = 0.18115$, *with the homoclinic tangle present. Panels* (b)–(d) *reflect different levels of zoom of the orbit in panel* (a). *(See movie in Figure* 14(a) *for an animation of the orbit.) Other parameters are as listed in the caption of Figure* 13. *(High resolution images zoom* 1000%.*)*

5. Discussion. This paper has concentrated on a particular case of stimulus-evoked, synchronous oscillations in two different spatially extended conductance-based neuronal network models that are driven by a time-independent, spatially localized excitatory current input. Ordered spatially along a one-dimensional continuum, the neurons in the neuronal medium are coupled via distance-dependent, homogeneous synaptic coupling that monotonically decays with the distance between pairs of cells. In both a purely inhibitory network and in an excitatory-inhibitory network with fast excitatory synapses, we demonstrated that, in the presence of a superthreshold current input, sufficiently strong synaptic inhibition is capable of generating a regular pattern of nearly synchronous action potentials occurring in a single continuous band of cells in each population, and the cycle-by-cycle evolution of the width of the band can exhibit behavior qualitatively similar to the dynamics of low-dimensional discrete maps. Subsequently, we derived heuristic one- and two-dimensional, implicit discrete

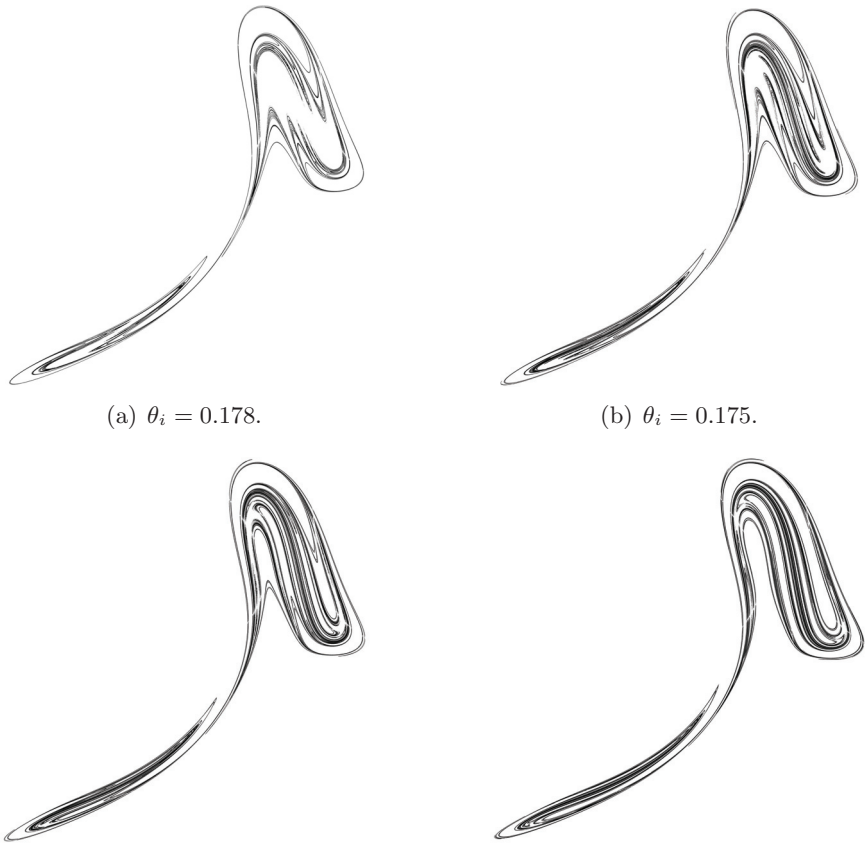

(a) $\theta_i = 0.178$. (b) $\theta_i = 0.175$.

(c) $\theta_i = 0.171$. (d) $\theta_i = 0.166$.

Figure 17. *The seahorse attractor for* $\sigma_{ii} = 1.5775$*, with other parameters as in Figure* 13(d)*. Each plot contains the orbits in the* (a_n, b_n) *plane of* 100 *closely spaced initial conditions, iterated* 1 *million times in parallel. The domain is* $[0, 1] \times [0, 3.5]$*. (High resolution images zoom* 1000%*.)*

maps that describe the cycle-by-cycle evolution of the width of the band of synchronous action potentials based upon (i) the current formulation of the conductance-based models and the exponential decay of synaptic transmission, (ii) the approximately periodic pattern of the oscillations, and (iii) the thresholding associated with action potential generation. Solutions of the discrete maps, when they existed, typically were single-valued on all iterates (though there were some exceptions). In some cases, various initial conditions failed to generate a solution or generated only a finite number of iterates, whereas other initial conditions were capable of being iterated indefinitely. This might be related to the observation in the conductance-based models that, in some cases, the initial or early stages of the transients did not always conform to the assumptions in the discrete maps.

We analyzed the bifurcation structure of the implicit discrete maps using linear stability analysis and compared it qualitatively with the simulations of the conductance-based models. Given the relatively fewer parameters in the inhibitory map, the comparison was more comprehensive, and we found that the bifurcation structures of the map and the conductance-

based model share strong similarities. Although the boundaries of the band of oscillations were assumed to evolve symmetrically about the input, we explored a two-dimensional map in which the boundaries are allowed to evolve independently. Linear stability analysis in this case indicates that stability of the fixed point is governed by the stability of symmetric perturbations, and the stability conditions are equivalent to the symmetric boundary case. Fast excitatory synaptic decay in the E-I conductance-based model similarly tended to result in dynamics approaching stable fixed points or period 2 orbits, which are typical solutions of the E-I map. Extending the decay time constant of synaptic excitation to be on the order of that of inhibition produced a wider range of the dynamics found in two-dimensional discrete maps, and a pair of related regions, in both the E-I map and E-I conductance-based model, exhibited Neimark–Sacker bifurcations with resonances in a transition zone leading to more complex oscillatory patterns. In fact, it was through explorations of parameter space in the E-I map that we identified this region in the conductance-based model. It would be interesting to explore the intricate dynamics common in this region of the conductance-based model to determine what other types of bifurcations occur and how they compare with the E-I map. However, high spatial and temporal resolution is necessary to resolve the dynamics accurately enough.

A number of improvements can be made to the heuristic maps. It would be interesting to try to determine a self-consistent relationship for the dependence of the thresholds θ_i and θ_e on other parameters of the map, given that the frequency of oscillation in the conductance-based model is an emergent property of the system. The parameters g_{uv} and θ_u also in theory could additionally depend on the cycle widths a_n, b_n to correct for the difference in cycle length. Inhibition was seen to have both an immediate effect and a long-term effect, which we incorporated implicitly as "early-cycle" inhibition in section 3.3. Synaptic excitation also has an early-cycle effect, as it rapidly stimulates and recruits more cells to fire in both populations, thereby widening the bands of spikes before the wave of inhibition precludes further firing. It would be interesting to explore other ways to formulate the map to capture the effects of early-cycle and late-cycle synaptic transmission in a manner that is consistent with the bifurcations exhibited by the conductance-based model; synaptic delays could even be introduced. One could further incorporate additional ionic currents or processes that affect the system on a longer time scale, for example, by introducing additional terms in the map that are analogous to the synaptic terms with an associated dynamic variable. Alternatively, the thresholds θ_i and θ_e could be taken to evolve dynamically on a longer time scale to reflect changes in the excitability of the populations. Finally, it would be interesting to extend the formulation of the map to describe more complex spatial patterns. For example, one could describe a solution which alternates between a single band and a pair of bands separated by a quiescent gap. Alternate iterates could track the different number of threshold points that define the alternating pattern. While it cannot be assumed that the entire course of a transient would follow such a prescription, it would be valid locally and would therefore be useful for determining the stability of such solutions.

As mentioned previously, in recordings of various cortical brain regions in vivo and via in vitro slice preparations, it is well known that excitatory neurons exhibit sparse irregular firing during gamma oscillations (i.e., cycle-skipping) in the range 4–12 spikes per second [28], which is in contrast to the periodic firing at gamma frequencies occurring herein. Although

it is possible to treat each point in the map or conductance-based model as an effective representation of a local population of neurons which as a whole is, in fact, seen to fire on each cycle in real brain tissue, the natural next step is to examine the case of sparse firing in the conductance-based models and its comparison with the discrete maps. In this first step in forming a concrete connection between the discrete maps and the conductance-based model, we have restricted simulations of the conductance-based model to the case of strong inhibition with regular firing so that the spatiotemporal patterns were clean and clearly relatable to the discrete map. The spatiotemporal patterns become more irregular in a gradual way as inhibition is weakened. Sparse firing generated by heterogeneity and/or noise in the neurons could also lead to irregularities in the patterns, requiring a thorough investigation and careful comparison with the solutions of the discrete maps. In this case, the synaptic strength parameters g_{uv} in the discrete map, for example, would be reinterpreted to reflect the current generated by the *fraction* of neurons firing on each cycle, whereas in our treatment they were related to the conductance-based model parameter g^c_{uv}, assuming that a continuous band of neurons fires on each cycle of the gamma oscillation. Similarly, the threshold currents θ_u would also need to be reinterpreted, since a neuron within the band of synchronous oscillations is assumed to fire on only a fraction of the gamma cycles.

Finally, we mention a possible relationship to the spatiotemporal dynamics described in [23], in which a spatially extended firing-rate neuronal network model was analyzed and compared with synchronous spiking in a conductance-based model. Their network is contrasted with ours in that it is defined on a one-dimensional ring network (periodic boundary conditions) with a spatially homogeneous current input and a Mexican hat synaptic weight function, and it also incorporates delays in the synaptic interactions. The oscillatory bump solutions in the firing-rate model relate to the fixed width/fixed point solutions in our treatment. However, in their spiking model, they find a localized oscillatory bump whose boundaries wander from cycle to cycle; though this could reflect an instability due to a bifurcation of the the fixed width solution, it could also be due to the noise that is present in the input. Other solutions deemed aperiodic patterns in the firing-rate model reveal oscillations in activity that alternate between two spatial bumps whose boundaries evolve in an aperiodic or quasi-periodic fashion. These patterns might be related to the weak resonances and periodic-like chaotic solutions described in the simulations of the E-I map.

Appendix A: Parameters for conductance-based models [8].

$$
\begin{aligned}
V_e^{\text{syn}} &= 0 \text{ mV}, & \alpha_m(v) &= 0.32(54+v)/(1-\exp(-(v+54)/4)),\\
V_i^{\text{syn}} &= -75 \text{ mV}, & \beta_m(v) &= 0.28(v+27)/(\exp((v+27)/5)-1),\\
V_{\text{Na}} &= +50 \text{ mV}, & \alpha_h(v) &= 0.128\exp(-(50+v)/18),\\
V_{\text{K}} &= -100 \text{ mV}, & \beta_h(v) &= 4/(1+\exp(-(v+27)/5)),\\
V_{\text{L}} &= -67 \text{ mV}, & \alpha_n(v) &= 0.032(v+52)/(1-\exp(-(v+52)/5)),\\
g_{\text{Na}} &= 100 \text{ mS/cm}^2, & \beta_n(v) &= 0.5\exp(-(57+v)/40),\\
g_{\text{K}} &= 80 \text{ mS/cm}^2, & \kappa(v) &= 1/(1+\exp(-(v+50))),\\
g_{\text{L}} &= 0.2 \text{ mS/cm}^2, & q_\infty(v) &= \alpha_q(v)/(\alpha_q(v)+\beta_q(v)), \quad p\in\{m,n,h\},\\
C &= 1\ \mu\text{F/cm}^2, & \tau_q(v) &= 1/(\alpha_q(v)+\beta_q(v)), \qquad q\in\{m,n,h\},\\
\alpha_i &= 12 \text{ ms}^{-1}, \quad \beta_i = 0.1 \text{ ms}^{-1}, & \alpha_e &= 1.1 \text{ ms}^{-1}, \quad \beta_e = 0.5 \text{ or } 0.123 \text{ ms}^{-1}.
\end{aligned}
$$

Appendix B: Linearization about the period 2 orbit in the E-I map. Expressions for the linearization about the two periodic points $(\bar{a}_1, \bar{b}_1)$ and $(\bar{a}_2, \bar{b}_2)$:

$$
\begin{aligned}
D_1F_e^{*1} &= D_1F_e(\bar{a}_1,\bar{b}_1,\bar{a}_2) &&= +D_2J_{ee}(\bar{a}_2,\bar{a}_1),\\
D_2F_e^{*1} &= D_2F_e(\bar{a}_1,\bar{b}_1,\bar{a}_2) &&= -D_2J_{ei}(\bar{a}_2,\bar{b}_1),\\
D_3F_e^{*1} &= D_3F_e(\bar{a}_1,\bar{b}_1,\bar{a}_2) &&= +D_1J_{ee}(\bar{a}_2,\bar{a}_1) - D_1J_{ei}(\bar{a}_2,\bar{b}_1) + I_e(\bar{a}_2),\\
D_1F_i^{*1} &= D_1F_i(\bar{a}_1,\bar{b}_1,\bar{b}_2) &&= +D_2J_{ie}(\bar{b}_2,\bar{a}_1),\\
D_2F_i^{*1} &= D_2F_i(\bar{a}_1,\bar{b}_1,\bar{b}_2) &&= -D_2J_{ii}(\bar{b}_2,\bar{b}_1),\\
D_3F_i^{*1} &= D_3F_i(\bar{a}_1,\bar{b}_1,\bar{b}_2) &&= +D_1J_{ie}(\bar{b}_2,\bar{a}_1) - D_1J_{ii}(\bar{b}_2,\bar{b}_1) + I_i(\bar{b}_2),\\
D_1F_e^{*2} &= D_1F_e(\bar{a}_2,\bar{b}_2,\bar{a}_1) &&= +D_2J_{ee}(\bar{a}_1,\bar{a}_2),\\
D_2F_e^{*2} &= D_2F_e(\bar{a}_2,\bar{b}_2,\bar{a}_1) &&= -D_2J_{ei}(\bar{a}_1,\bar{b}_2),\\
D_3F_e^{*2} &= D_3F_e(\bar{a}_2,\bar{b}_2,\bar{a}_1) &&= +D_1J_{ee}(\bar{a}_1,\bar{a}_2) - D_1J_{ei}(\bar{a}_1,\bar{b}_2) + I_e(\bar{a}_1),\\
D_1F_i^{*2} &= D_1F_i(\bar{a}_2,\bar{b}_2,\bar{b}_1) &&= +D_2J_{ie}(\bar{b}_1,\bar{a}_2),\\
D_2F_i^{*2} &= D_2F_i(\bar{a}_2,\bar{b}_2,\bar{b}_1) &&= -D_2J_{ii}(\bar{b}_1,\bar{b}_2),\\
D_3F_i^{*2} &= D_3F_i(\bar{a}_2,\bar{b}_2,\bar{b}_1) &&= +D_1J_{ie}(\bar{b}_1,\bar{a}_2) - D_1J_{ii}(\bar{b}_1,\bar{b}_2) + I_i(\bar{b}_1).
\end{aligned}
$$

Acknowledgments. S. Folias would like to thank Nancy Kopell for inspiring his interest in gamma oscillations and G. R. Hall for helpful comments. The authors would also like to thank the referees for providing helpful comments and suggestions.

REFERENCES

[1] V. I. Arnold, *Geometrical Methods in the Theory of Ordinary Differential Equations*, 2nd ed., Springer-Verlag, New York, 1988.

[2] D. G. Aronson, M. Chory, G. R. Hall, and R. P. McGehee, *Bifurcations from an invariant circle for two-parameter families of maps of the plane: A computer assisted study*, Comm. Math. Phys., 83 (1982), pp. 303–354.

[3] D. K. Arrowsmith, J. H. E. Cartwright, A. N. Landsbury, and C. M. Place, *The Bogdanov map: Bifurcations, mode locking, and chaos in a dissipative system*, Internat. J. Bifur. Chaos Appl. Sci. Engrg., 3 (1993), pp. 2086–2096.

[4] D. K. Arrowsmith and C. M. Place, *An Introduction to Dynamical Systems*, 2nd ed., Cambridge University Press, Cambridge, UK, 1990.

[5] C. Börgers and N. Kopell, *Effects of noisy drive on rhythms in networks of excitatory and inhibitory neurons*, Neural Comput., 17 (2005), pp. 557–608.

[6] A. Compte, N. Brunel, P. C. Goldman-Rakic, and X.-J. Wang, *Synaptic mechanisms and network dynamics underlying spatial working memory in a cortical network model*, Cerebral Cortex, 10 (2000), pp. 910–923.

[7] S. Coombes and P. C. Bressloff, *Mode-locking and Arnold tongues in integrate-and-fire neural oscillators*, Phys. Rev. E, 60 (1999), pp. 2086–2096.

[8] G. B. Ermentrout, *The analysis of synaptically generated traveling waves*, J. Comput. Neurosci., 5 (1998), pp. 191–208.

[9] G. B. Ermentrout and N. Kopell, *Fine structure of neural spiking and synchronization in the presence of conduction delays*, Proc. Natl. Acad. Sci. USA, 95 (1998), pp. 1259–1264.

[10] S. E. Folias and P. C. Bressloff, *Breathing pulses in an excitatory neural network*, SIAM J. Appl. Dyn. Syst., 3 (2004), pp. 378–407.

[11] S. E. Folias and P. C. Bressloff, *Breathing pulses in two-dimensional neural media*, Phys. Rev. Lett., 95 (2005), paper 208107.

[12] V. S. Gonchenko, Yu. A. Kuznetsov, and H. G. E. Meijer, *Generalized Hénon map and bifurcations of homoclinic tangencies*, SIAM J. Appl. Dyn. Syst., 4 (2005), pp. 407–436.
[13] C. M. Gray and W. Singer, *Stimulus-specific neuronal oscillations in orientation columns of cat visual cortex*, Proc. Natl. Acad. Sci. USA, 86 (1989), pp. 1698–1702.
[14] J. Gukenheimer and P. Holmes, *Nonlinear Oscillations, Dynamical Systems, and Bifurcations of Vector Fields*, Springer-Verlag, New York, 1983.
[15] D. Johnston and W.-S. Wu, *Foundations of Cellular Neurophysiology*, 3rd ed., MIT Press, Cambridge, MA, 1997.
[16] C. Koch and I. Segev, *Methods in Neuronal Modeling, From Ions to Networks*, 2nd ed., MIT Press, Cambridge, MA, 1999.
[17] Y. A. Kuznetsov, *Elements of Applied Bifurcation Theory*, 3rd ed., Springer-Verlag, New York, 2004.
[18] Y. A. Kuznetsov, H. G. E. Meijer, and L. Van Veen, *The fold–flip bifurcation*, Internat. J. Bifur. Chaos Appl. Sci. Engrg., 14 (2004), pp. 2253–2282.
[19] Yu. A. Kuznetsov and H. G. E. Meijer, *Numerical normal forms for codim 2 bifurcations of fixed points with at most two critical eigenvalues*, SIAM J. Sci. Comput., 26 (2005), pp. 1932–1954.
[20] T. LoFaro and N. Kopell, *Timing regulation in a network reduced from voltage-gated equations to a one-dimensional map*, J. Math. Biol., 38 (1999), pp. 479–533.
[21] D. McMillen and N. Kopell, *Noise-stabilized long-distance synchronization in populations of model neurons*, J. Comput. Neurosci., 15 (2003), pp. 143–157.
[22] D. D. Pervouchine, T. I. Netoff, H. G. Rotstein, J. A. White, M. O. Cunningham, M. A. Whittington, and N. Kopell, *Low dimensional maps encoding dynamics in the entorhinal cortex and hippocampus*, Neural Comput., 18 (2006), pp. 2617–2650.
[23] A. Roxin, N. Brunel, and D. Hansel, *Role of delays in shaping spatiotemporal dynamics of neuronal activity in large networks*, Phys. Rev. Lett., 94 (2005), paper 238103.
[24] F. Takens, *Forced oscillations and bifurcations*, Comm. Math. Inst. Rijkuniversiteit Utrecht, 3 (1974), pp. 1–59.
[25] X.-J. Wang and G. Buzsáki, *Gamma oscillation by synaptic inhibition in a hippocampal interneuronal network model*, J. Neurosci., 16 (1996), pp. 6402–6413.
[26] D. Whitley, *Discrete dynamical systems in degrees one and two*, Bull. London Math. Soc., 373 (1983), pp. 177–217.
[27] M. A. Whittington, R. D. Traub, and J. G. Jefferys, *Synchronized oscillations in interneuron networks driven by metabotropic glutamate receptor activation*, Nature, 373 (1995), pp. 612–615.
[28] M. A. Whittington, R. D. Traub, N. Kopell, G. B. Ermentrout, and E. H. Buhl, *Inhibition-based rhythms: Experimental and mathematical observations on network dynamics*, Int. J. Psychophysiol., 38 (2000), pp. 315–336.
[29] H. R. Wilson and J. D. Cowan, *A mathematical theory of the functional dynamics of cortical and thalamic nervous tissue*, Kybernetik, 13 (1973), pp. 55–80.